AFOSR-TR- 92 0[illegible]

HAC REF G8200

AD-A250 710

ELECTROMAGNETIC-WAVE PROPAGATION IN UNMAGNETIZED PLASMAS

DTIC
ELECTE
MAY 18 1992
S D

D.J. Gregoire, J. Santoru and R.W. Schumacher
Hughes Research Laboratories
3011 Malibu Canyon Rd.
Malibu, CA 90265

March 1992

F49620-89-C-0063
Final Report
May 1, 1989 through January 31, 1992

DISTRIBUTION STATEMENT A
Approved for public release
Distribution Unlimited

Prepared for
AIR FORCE OFFICE OF SCIENTIFIC RESEARCH
Bolling Air Force Base
Washington, DC 20332-6448

92-13065

REPORT DOCUMENTATION PAGE

Form Approved
OMB No 0704-0188

Public report ing burden for this collection of information is estimated to average hour per response, including the time for review ing instruct ions, search ing existing data sources, gather ing and maintain ing the data needed, and complet ing and review ing the collect ion of information. Send comments regarding this burden estimate or any other aspect of this collection of information, including suggestions for reducing this burden, to Washington Headquarters Services, Directorate for information Operations and Reports, 1215 Jefferson Davis Highway, Suite 1204, Arlington, VA 22202-4302, and to the Office of Management and Budget, Paperwork Reduction Project (0704-0188), Washington, DC 20503.

1. AGENCY USE ONLY (Leave blank)	2. REPORT DATE	3. REPORT TYPE AND DATES COVERED
	31 March 1992	Final 89/5/1 to 92/1/31

4. TITLE AND SUBTITLE
Electromagnetic Wave Propagation in Unmagnetized Plasmas

5. FUNDING NUMBERS
F49620-89-C-0063

6. AUTHOR(S)
Daniel J. Gregoire, Joseph Santoru, Robert W. Schumacher

7. PERFORMING ORGANIZATION NAME(S) AND ADDRESS(ES)
Hughes Research Laboratories
3011 Malibu Canyon Road
Malibu, CA 90265

8. PERFORMING ORGANIZATION REPORT NUMBER

9. SPONSORING / MONITORING AGENCY NAME(S) AND ADDRESS(ES)
Air Force Office of Scientific Research
Bolling Air Force Base, Bldg. 410
Washington, DC 20332-6448

10. SPONSORING / MONITORING AGENCY REPORT NUMBER
2301 A5

11. SUPPLEMENTARY NOTES

12a. DISTRIBUTION / AVAILABILITY STATEMENT
unlimited

12b. DISTRIBUTION CODE

13. ABSTRACT (Maximum 200 words)

This final report describes an investigation of electromagnetic-wave propagation in unmagnetized plasmas and its application to the reduction of the radar cross section (RCS) of a plasma-filled enclosure. We have demonstrated RCS reduction of 20 to 25 dB with a prototype system at the radar range at Hughes Aircraft's Microwave Products Division in Torrance. The prototype consists of a sealed ceramic enclosure with a microwave reflector and a plasma generator inside it. When the plasma is present, the RCS is significantly reduced over a frequency range of 4 to 14 GHz. As part of the program, we also investigated the basic-plasma-physics issues relating to the absorption and refraction of electromagnetic (EM) waves in collisional plasmas. We demonstrated absorption as high as 63 dB in a section of plasma-loaded C-band rectangular waveguide. We also developed a theoretical model for the plasma cloaking process that includes scattering contributions from the plasma-vacuum interface, partial reflections from the plasma, and collisional absorption in the plasma. The theoretical model is found to be in reasonable agreement with the experimental results and can be used to confidently design future plasma cloaking systems.

14. SUBJECT TERMS	15. NUMBER OF PAGES
Plasma Cloaking, RCS Reduction	66
	16. PRICE CODE

17. SECURITY CLASSIFICATION OF REPORT	18. SECURITY CLASSIFICATION OF THIS PAGE	19. SECURITY CLASSIFICATION OF ABSTRACT	20. LIMITATION OF ABSTRACT
Unclassified	Unclassified	Unclassified	UL

TABLE OF CONTENTS

For
Availability Codes
Dist Special
A-1

LIST OF FIGURES

1. INTRODUCTION

This final report describes an investigation of electromagnetic-wave propagation in unmagnetized plasmas and its application to the reduction of the radar cross section (RCS) of a plasma-filled enclosure. Such RCS reduction is an example of *plasma cloaking* where artificially-produced plasmas act as EM-wave absorbers or refractors. Figure 1 illustrates schematically these two cloaking scenarios. We have demonstrated RCS reduction of 20 to 25 dB with a prototype system at the radar range at Hughes Aircraft's Microwave Products Division in Torrance. The prototype consists of a sealed ceramic enclosure with a microwave reflector and a plasma generator inside it. When the plasma is present, the RCS is significantly reduced over a frequency range of 4 to 14 GHz. The plasmas are produced by a seed-gas/UV photoionization technique that permits independent variation of the plasma-density profile and the electron-collision frequency. As part of the program, we also investigated the basic-plasma-physics issues relating to the absorption and refraction of electromagnetic (EM) waves in collisional plasmas. We demonstrated absorption as high as 63 dB in a section of plasma-loaded C-band rectangular waveguide. We also developed a theoretical model for the plasma cloaking process that includes scattering contributions from the plasma-vacuum interface, partial reflections from the plasma, and collisional absorption in the plasma. The theoretical model is found to be in reasonable agreement with the experimental results and can be used to confidently design future plasma cloaking systems.

Based on the RCS reduction, plasma cloaking could be used to shield parts of existing vehicles having large radar cross sections without major structural alterations. Costly redesigns could be delayed and the equipment's service lifetime within the arena of electronic warfare would be extended. One major advantage of plasma cloaking over conventional stealth technologies is that the plasma can be implemented as a "shuttered" cloaking system that is switched on and off very rapidly. The plasma would cloak the electromagnetic transmission systems by rapidly turning on the plasma when the communication or radar systems were not transmitting or receiving. Different plasma cloaking systems could be developed for use on ships, airborne platforms, and satellites to provide protection against different radar threats.

An effective plasma cloaking system successfully absorbs and/or refracts the incident radiation to such an extent that the returned signal is obscured by background noise. An inhomogeneous, unmagnetized, collisional plasma[1-4] can efficiently absorb electromagnetic waves. The EM-wave fields accelerate the plasma electrons which collide

a.) EM wave is attenuated by the plasma as it is reflected from the target.

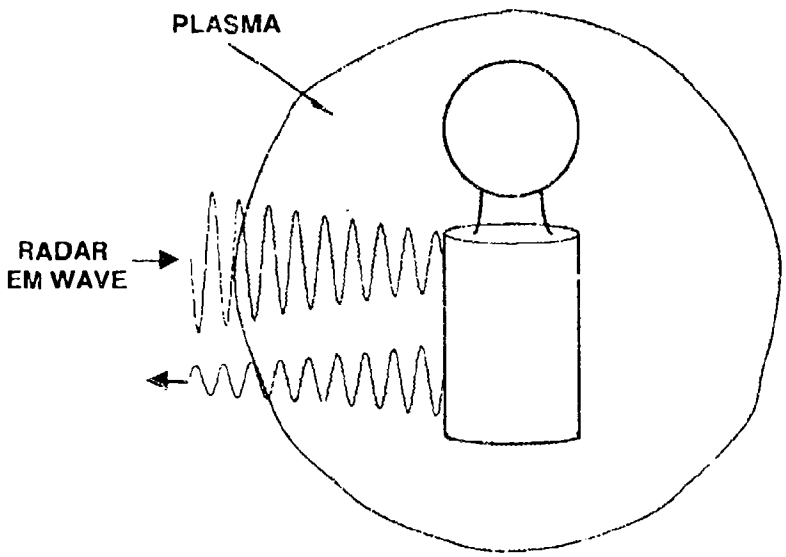

b.) EM wave is refracted around the cloaked target.

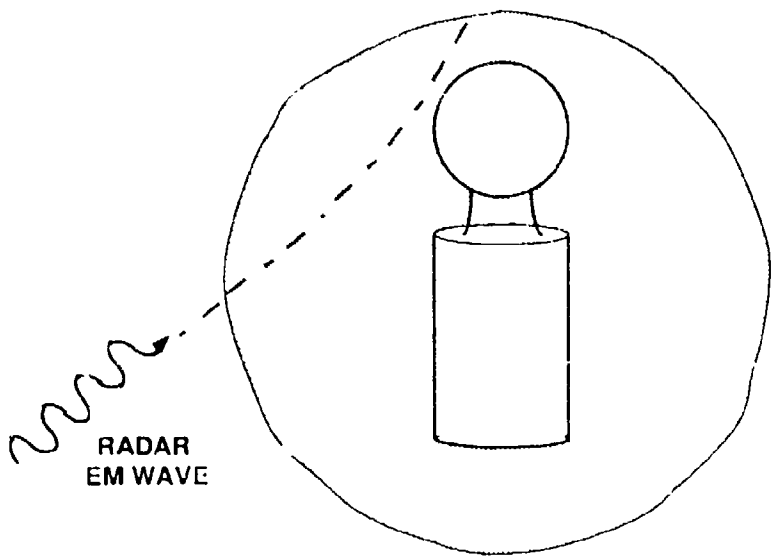

Figure 1 Plasma-cloaking scenarios.

with the background gas molecules, thereby transferring energy from the EM wave to the gas. In the absorptive plasma-cloaking scenario, shown in Figure 1a, where a target is surrounded by tan absorptive plasma, the EM-wave makes two passes through the plasma as it irradiates and is reflected from the target, losing energy in each pass. The total RCS reduction in this scenario is dependent on several parameters such as the plasma volume, the EM-wave frequency, the momentum-transfer collision frequency, and the plasma density. In the refractive plasma-cloaking scenario, shown in Figure 1b, the incident EM-wave is scattered by the changing dielectric constant within the plasma, thus minimizing the interaction with the target.

1.1 Summary of Experimental Results

Hughes approach to the investigation of plasma cloaking during the first year of our program was to measure the transmission and reflection of EM-waves propagating in a section of plasma-loaded rectangular waveguide and their variance as functions of the plasma-density profile and momentum-transfer collision rate. Experimental results were compared with the theoretical model.

Significant theoretical and experimental progress has been made during the course of our program. The following items describe our results during the first year.

- Assembled glass-"T" vacuum vessel, mechanical vacuum pump, and seed-gas and background-gas flow and monitoring system.
- Assembled spark-gap modulator with 15-kV high-voltage power supply and ignitron switch.
- Fabricated and operated preliminary three-gap spark array with tungsten electrodes.
- Demonstrated plasma production using UV-photoionization of an Ar/He seed/background-gas mixture.
- Fabricated and cold-tested C-band waveguide section with 75% transparent sidewalls with performance accurately predicted by theoretical analyses.
- Assembled and operated EM-wave transmission and monitoring network.
- Measured 63 dB maximum attenuation for 4-GHz signal transmitted through plasma. The same plasma profile provides ≥38 dB from 4 through 6 GHz, thereby validating the broadband absorber concept.

- Measured attenuation as functions of collision frequency and plasma density (i.e., spark-gap current). The scaling is consistent with our absorption model.

During the second year, we applied the knowledge we gained from the first year experiments on plasma production and EM-wave absorption to the development and demonstration of a plasma-cloaking prototype. The second-year milestones are listed below.

- Assembled ceramic enclosure with perforated microwave reflector and spark-gap array.
- Ensured proper operation of plasma-generation mechanism within the ceramic enclosure.
- Measured up to 37 dB attenuation of reflected microwave signal from the plasma-filled enclosure in laboratory-based two-horn microwave scattering experiments.
- Measured RCS reduction (RCSR) of the plasma-filled enclosure using the compact radar range at Hughes-MPD. The RCSR was from 20 to 25 dB over the frequency range of 4 to 14 GHz.
- Compared RCSR measurements to a theoretical one-dimensional plasma-filled enclosure model.

In the following sections we will review our technical progress in understanding and demonstrating the basic physics of collisional EM-wave absorption and its application to the plasma-cloaking prototype. In Section 2 we present the theoretical considerations for our program starting with a simple absorption model of a plasma-cloaked target. Important topics include quantification of reflection from a plasma-vacuum interface, propagation in a plasma-filled waveguide and the physics of the plasma-filled Fabry-Perot resonator as it relates to multiple reflections in the plasma-filled enclosure. Section 3 follows with discussions related to the program's experimental design aspects. Foremost among these is the plasma-production technique. In Section 4 we present our results from the plasma-filled waveguide experiments, including attenuation scaling with radiation frequency, momentum-transfer collision frequency and plasma density. The results are compared to the predictions of the model treated in Section 2. Finally in Section 5, we present the details of the RCSR measurements made of the plasma-filled ceramic enclosure at the Hughes-MPD radar range.

2. THEORY OF EM-WAVE PROPAGATION IN AN UNMAGNETIZED PLASMA

2.1. Basic Theory

In the analysis throughout this section, we assume that the electron-neutral collision frequency in the plasma is such that the mean free path between collisions is much smaller than the Debye length. Thus, any collective plasma interactions are effectively quenched by collisions. This is equivalent to requiring that the electron temperature is very small. If this were not the case, then it would be possible for EM-waves to lose energy to the plasma by exciting electrostatic waves [5]. Therefore, barring any interaction with plasma waves, an EM-wave will pass through a uniform, collisionless, unmagnetized plasma without any attenuation provided the EM-wave angular frequency ω_0, exceeds the plasma frequency defined by $\omega_p(z) = [n_e e^2/m_e\varepsilon_0]^{1/2}$, where m_e is the electron mass, e is the electron charge, ε_0 is the free-space permittivity, and n_e is the plasma-electron density. In the case where the radiation is incident on an overdense plasma such that $\omega_p > \omega_0$, the EM-wave is totally reflected. If the plasma density varies with the longitudinal coordinate z, then the wave is totally reflected at the point where the plasma density exceeds a critical value determined by $\omega_p = \omega_0$.

In contrast to the collisionless plasma, a collisional plasma will attenuate an EM-wave; also the wave will never be totally reflected because the collisions modify the propagation constant to be complex, thus preventing the real part from vanishing in an overdense plasma. The dielectric constant for an unmagnetized, cold (i.e., $T_e = 0$) plasma can be derived from the Lorentz equation of motion [6],

$$m_e \frac{d^2\mathbf{r}}{dt^2} = -e\mathbf{E} - \nu_c m_e \frac{d\mathbf{r}}{dt} \quad , \tag{1}$$

where $\boldsymbol{r}$ is the three-dimensional electron position vector, $\boldsymbol{E}$ is the electric field of the EM wave, ν_c is the electron electron-neutral collision frequency, and $i = (-1)^{1/2}$. Using $\boldsymbol{E} \propto \boldsymbol{E}_0 exp(i\omega_0 t)$ we can solve for $\boldsymbol{r}$,

$$\mathbf{r} = \frac{e\mathbf{E}}{m_e\omega_0(\omega_0 - i\nu_c)} \quad . \tag{2}$$

If we consider the one-dimensional case where the plasma density varies only in the z-direction, the conductivity σ_c can be written as

$$\sigma_c = -\frac{n_e e}{E}\frac{dr}{dt} = \frac{n_e e^2}{m_e}\frac{\nu_c - i\omega_o}{\omega_o^2 + \nu_c^2} \quad . \tag{3}$$

In general, the electron density in this expression is a function of the spatial position, $n_e = n_e(z)$. The dielectric constant ε may be written in terms of the conductivity as

$$\varepsilon = 1 - \frac{i\sigma_c}{\varepsilon_o \omega_o} \quad , \tag{4}$$

Therefore, the dielectric constant ε_p for an collisional, unmagnetized, cold plasma is complex and has the form

$$\varepsilon_p = 1 - \frac{\omega_p^2}{\left(\omega_o^2 + \nu_c^2\right)} - i\frac{\nu_c}{\omega_o}\frac{\omega_p^2}{\left(\omega_o^2 + \nu_c^2\right)} \quad . \tag{5}$$

When $\nu_c=0$, Equation (5) reduces to the well known expression for the dielectric constant of a collisionless plasma $\varepsilon_p = \left(1 - \omega_p^2/\omega_o^2\right)$ which goes negative in an overdense plasma. The propagation constant (k) for an EM-wave in the collisional plasma is complex

$$k = k_o\sqrt{\varepsilon_p} = k_r + ik_i \quad , \tag{6}$$

where $k_o \equiv \omega_o/c$ is the free-space wavenumber, and k_r and k_i are the real and imaginary parts of the wavenumber, respectively. It is not possible for either part of k to vanish except when $\nu_c=0$. Solving Equation (6) for the real and imaginary parts of k yields

$$k_r = k_o\, r\cos(\phi/2) \tag{7}$$

and

$$k_i = k_o\, r\sin(\phi/2) \tag{8}$$

respectively, where r and ϕ are defined as

$$r = \left\{1 - \frac{\omega_p^2}{\omega_o^2 + \nu_c^2}\left(2 - \omega_p^2/\omega_o^2\right)\right\}^{1/4} \tag{9}$$

and

$$\phi = \begin{cases} \phi_0 & ; \quad \mathrm{Re}(\varepsilon) > 0 \\ \phi_0 + \pi & ; \quad \mathrm{Re}(\varepsilon) < 0 \end{cases} \tag{10}$$

given the definition for the phase

$$\phi_0 \equiv \tan^{-1}\left[-\nu_c\omega_p^2 \Big/ \omega_o\left(\omega_o^2 + \nu_c^2 - \omega_p^2\right)\right] .$$

The real part of k, k_r, indicates the EM-wave's rate of spatial oscillation while the imaginary part of k, k_i, expresses the field's decay rate as the wave moves through the absorptive medium.

2.2. Collisional Absorption by a Plasma

Electromagnetic-wave propagation in a dielectric media is governed by the wave equation

$$\frac{d^2E(z)}{dz^2} + k^2(z)E(z) = 0 \tag{11}$$

We employ the WKB method[7] to derive an approximate solution,

$$E(z) = E_o \exp\left[i \int_0^z k(z')dz' \right] , \tag{12}$$

which is valid in any region where

$$\frac{1}{k^2}\frac{dk}{dz} \ll 1 \tag{13}$$

which requires that the wavenumber change very little over a distance of one wavelength. This condition is easily satisfied by all but the sharpest plasma gradients, or when the wavenumber approaches zero (i.e., at waveguide cutoff).

2.2.1. Attenuation in a uniform plasma

For an infinite plasma of uniform density, Equation (12) yields an expression for the EM-wave power as a function of distance

$$P(z) = P_o e^{-i2k_i z} \quad , \tag{14}$$

where P_o is the power at $z = 0$. The expression can be rearranged to yield a formula for the attenuation in the medium

$$Attenuation\ /cm = [2 \times 10\log_{10}(e)]k_i \tag{15}$$

Therefore the attenuation is proportional to the imaginary part of the propagation constant of Equation (6). The form of k_i given in Equation (8) does not lend itself to easy analysis. It is useful to examine the form of k in the extreme limits where $\nu_c \to 0$ and $\nu_c >> \omega_o, \omega_p$.

$$\lim_{\nu_c >> \omega_p, \omega_o} k = k_o \left[\left(1 + \frac{1}{2} \frac{\omega_p^2}{\nu_c^2} \left(\frac{\omega_p^2}{4\omega_o^2} - 1 \right) \right) - i \frac{\omega_p^2}{\nu_c \omega_o} \left(1 - \frac{\omega_0^2 - 4\omega_p^2}{\nu_c^2} \right) \right] \tag{16}$$

$$\lim_{\nu_c \to 0} k = \begin{cases} k_o \sqrt{1 - \omega_p^2/\omega_o^2} \left(1 - i \frac{1}{2} \frac{\omega_p^2}{\omega_o \left(\omega_o^2 - \omega_p^2 \right)} \nu_c \right) & ; \quad \omega_o > \omega_p \\ k_o \sqrt{\omega_p^2/\omega_o^2 - 1} \left(i - \frac{1}{2} \frac{\omega_p^2}{\omega_o \left(\omega_p^2 - \omega_o^2 \right)} \nu_c \right) & ; \quad \omega_o < \omega_p \end{cases} \tag{17}$$

From Equations (16) and (17), it is seen that the imaginary part of the propagation constant vanishes as the collision frequency approaches the extreme limits of zero or infinity given the condition that $\omega_p < \omega_o$. Figure 2 plots the absorption constant in dB/cm for EM-waves of various frequencies propagating in a uniform plasma. As predicted by Equations (16) and (17), Figure 2 shows that the absorption tends to zero as the collision frequency approaches the extreme limits except when $\omega_o < \omega_p$. Furthermore and most importantly, there is a peak in the absorption when $\nu_c \sim \omega_o$. These features are easily understood in terms of the simple model of a plasma electron being oscillated by an EM wave and impeded by collisions with background atoms. As the EM-wave moves into the plasma, its electric field oscillates the electrons. If there are no collisions, the electrons act as a lossless dielectric. However, when a collection of neutral background atoms are present, the electrons will collide with and transfer their kinetic energy to the background atoms. The energy transfer is critically dependent on the phase of the electron's oscillation

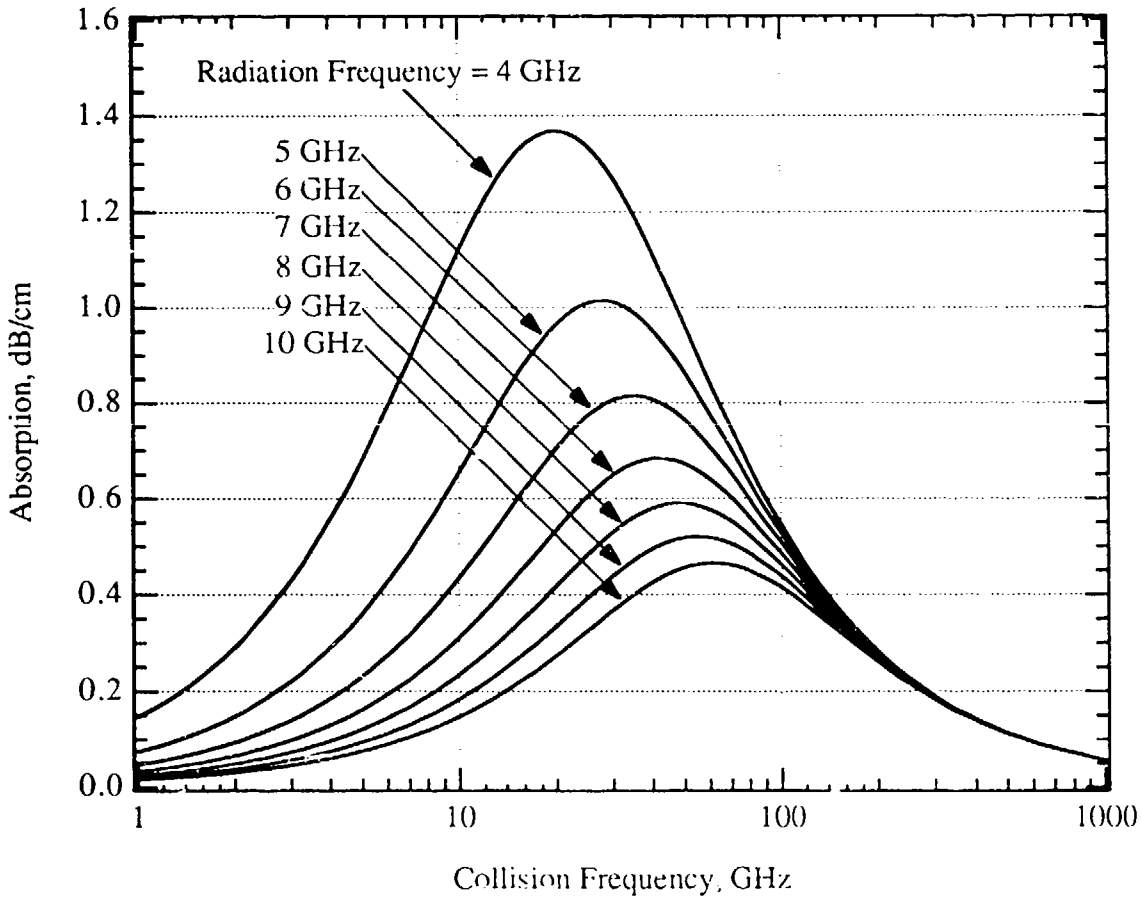

Figure 2 Attenuation of EM wave by collisional absorption in a uniform plasma with f_p = 3.2 GHz corresponding to a plasma density of 10^{11} cm^{-3}. Figure 2 plots the absorption vs collision frequency for a number of radiation frequencies. The curves show that the absorption reaches a peak when the collision frequency is near the radiation frequency.

cycle when the collision occurs. If an electron suffers a collision when it has maximum kinetic energy (at a quarter way through its oscillation cycle), then the energy transfer is most efficient. Therefore we can expect the net energy transfer to be the maximum when the collision rate is roughly equal to the EM-wave frequency and a requirement for good absorption is $\nu_c \sim \omega_0$.

When $\nu_c >> \omega_o$, the absorption properties are very poor because the electrons have acquired very little energy before they collide with neutrals. This is verified by Equation (16) which shows that $k_i \sim 1/\nu_c$ in the limit of large ν_c. In the limit of $\nu_c << \omega_o$, the collision rate is so low that the electrons simply oscillate in the EM-wave fields unimpeded and little energy is dissipated.

2.2.2. Attenuation in a non-uniform plasma

To find the wave attenuation in a non-uniform plasma, we use Equation (12) and calculate the integral over the EM-wave's path. For an EM wave which enters a plasma at $z = z_0$, propagates to a reflecting target at $z = z_1$, and then returns through the plasma, we estimate according to the WKB approximation that the net reflected power is

$$P = P_o \exp\left\{-4\int_{z_o}^{z_1} \mathrm{Im}[k(z')]dz'\right\} \tag{18}$$

and the attenuation in dB is

$$\text{Attenuation(dB)} = 17.36\int_{z_o}^{z_1} \mathrm{Im}[k(z')]dz' \tag{19}$$

2.2.3. Attenuation in a plasma-loaded waveguide

It is much easier to make EM-wave transmission and reflection measurements if they are done in a transmission line or waveguide rather than in free space. In our investigation of the effects of plasmas on EM-wave propagation, we have used a waveguide to perform the measurements. Therefore it is important to understand the differences between the plasma attenuation in the waveguide and free space.

In the waveguide, the complex propagation constant k becomes

$$k^2 = \varepsilon_p(z)k_o^2 - k_c^2 \tag{20}$$

where k_c is the vacuum cutoff wavenumber of the waveguide. For a collisionless plasma, the EM-wave propagation constant is equivalent to that in a waveguide with cutoff wavenumber equal to $\sqrt{k_c^2 + (\omega_p/c)^2}$. As in free space propagation through a plasma, the effect of collisions is to remove the possibility of $k_r=0$, thus eliminating the phenomenon of total reflection at the cutoff frequency.

The absorption calculations now proceed in the same manner as before, except with Equation (20) used as the wavenumber. Figure 3 compares the attenuation for a uniform plasma in free space and a C-band rectangular waveguide. It is evident that the absorption is always higher in the waveguide given the same plasma and radiation parameters. This difference is more pronounced as the radiation frequency approaches the waveguide's cutoff frequency.

2.3. Reflections from a Plasma-Cloaked Target

Figure 4 illustrates the standard plasma-cloaking scenario. A highly reflective target located at $z=z_1$ is surrounded by a plasma which extends from $z=z_0$ to the target. As shown in the figure, the plasma typically reaches maximum density at the target and gradually decreases in intensity as a function of distance from the target. The density also suffers a sharp decrease to $n_e=0$ at $z=z_0$ due to the walls of a plasma confinement vessel. There are three contributions to the reflected EM-wave power in this scenario

1) Reflections from the vacuum-plasma interface. Some power will be reflected at the media discontinuity.
2) Partial reflections from the bulk plasma volume. These are EM waves that are weakly reflected from the plasma density gradient.
3) Target reflection. This is the EM-wave power that is reflected from the target, while being attenuated by collisional absorption in the plasma.

The relative values of these reflected powers determines which of them is the limiting factor for RCS reduction. For example, it is pointless to attenuate the target reflections to be negligible compared to the other reflections since the RCS reduction is determined by the combination of the all the reflections.

2.3.1. Reflection from a sharp vacuum-plasma interface

Figure 4 shows an EM wave incident on a plasma with a sharp boundary at $z = z_0$. The power reflected from a sharp plasma-vacuum interface can be computed by the Fresnel formula

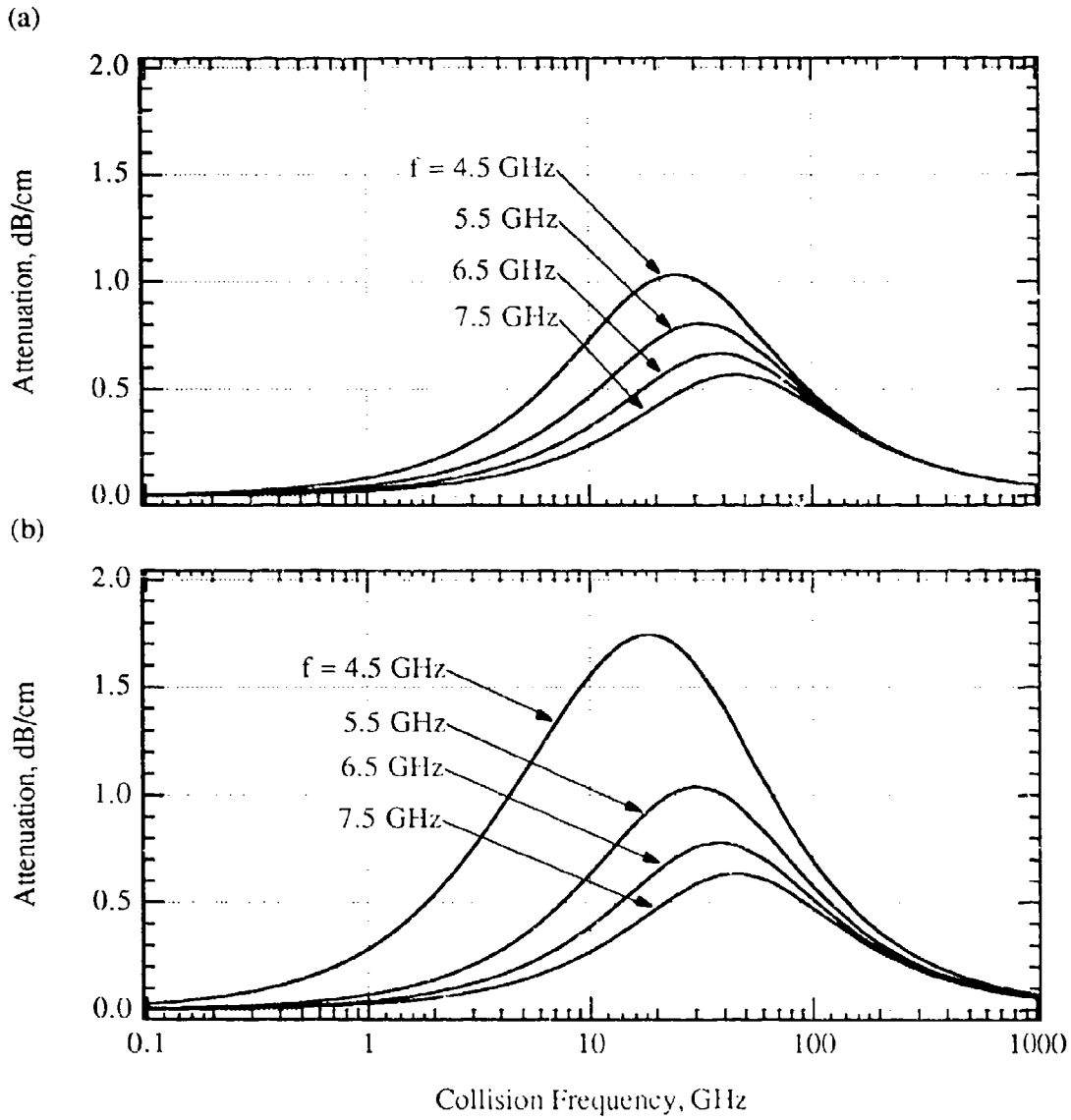

Figure 3 Attenuation of EM wave transmitted through (a) a free-space plasma, and (b) a plasma-loaded C-band waveguide with a 3.2-GHz vacuum cutoff frequency. The EM-wave frequencies range from 4.5 to 7.5 GHz and the plasma frequency is 3 GHz. The absorption is greater in the waveguide and the optimum collision frequency is shifted to lesser values.

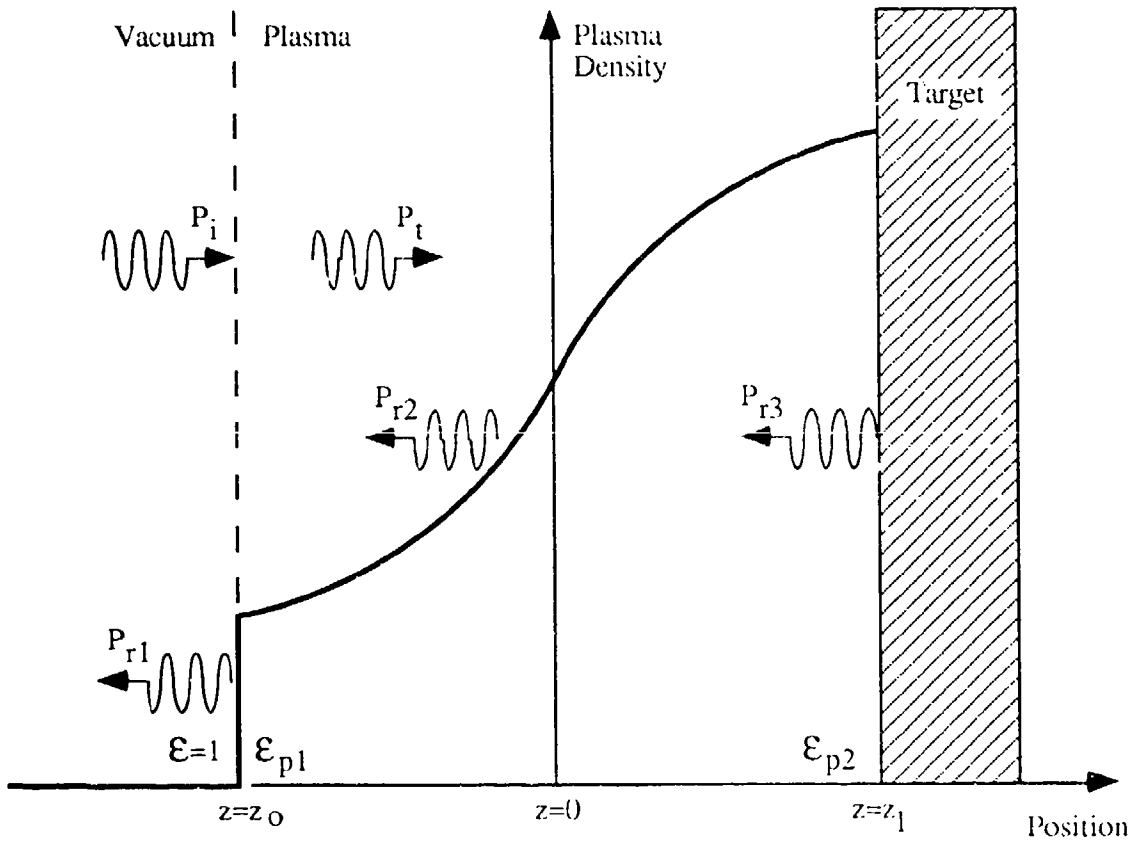

Figure 4 A target surrounded by a plasma with an Epstein profile. The incident EM-wave power is reflected by the plasma-vacuum interface (P_{r1}), the density gradient in the bulk plasma (P_{r2}), and by the target (P_{r3}).

$$\frac{P_{rl}}{P_i} = \left| \frac{1 - \sqrt{\varepsilon_{pl}}}{1 + \sqrt{\varepsilon_{pl}}} \right|^2 \quad , \tag{21}$$

where P_{rl} is the reflected power, P_i is the incident power and ε_{pl} is the plasma dielectric constant at $z = z_0$. Figure 5a the shows the scaling of the reflected power vs f_o/f_p $(= \omega_o/\omega_p)$ as given by Equation (21). For the collisionless plasma, total reflection occurs when $\omega_o/\omega_p \leq 1$, and the reflected power drops for $\omega_o/\omega_p > 1$. When collisions are included, the wave always penetrates into the plasma and is attenuated by the plasma. The reflected power is greatly reduced as ν_c increases , even when $\omega_o/\omega_p \geq 1$. In conclusion, it is routine to reduce the refection from the interface by 30 dB or more by judicious choices of the plasma parameters.

2.3.2. Reflections from the plasma density gradient

The fraction of the EM-wave power (P_i) that penetrates beyond the vacuum-plasma interface is partially reflected by density gradients in the plasma volume. Although this process can be treated numerically, exact solutions to the EM-wave differential equation may be obtained for certain density profiles. One such profile is the Epstein plasma-density profile given by

$$n_e(z) = n_0(1 + e^{-z/\sigma}) \quad . \tag{22}$$

where n_0 is the peak electron density at $z = +\infty$ and σ is the scale length of the gradient. An example of the Epstein profile is shown in Figure 6 for different values of σ. The power reflection coefficient for normal incidence[8] is

$$R = \left| \frac{1 - \varepsilon^{1/2}}{1 + \varepsilon^{1/2}} \right|^2 \left| \frac{\Gamma\left[1 + ik\sigma\left(\varepsilon^{1/2} + 1\right)\right]}{\Gamma\left[1 + ik\sigma\left(\varepsilon^{1/2} - 1\right)\right]} \right|^4 \quad , \tag{23}$$

where Γ is the complex gamma function and ε is the plasma dielectric constant evaluated at infinity. If $\sigma = 0$, then Equation (23) reduces to the Fresnel formula of Equation (21).

In the scenario of Figure 4 the plasma has much less than infinite extent, however we argue that Equation (23) will give good approximate results for the density-gradient

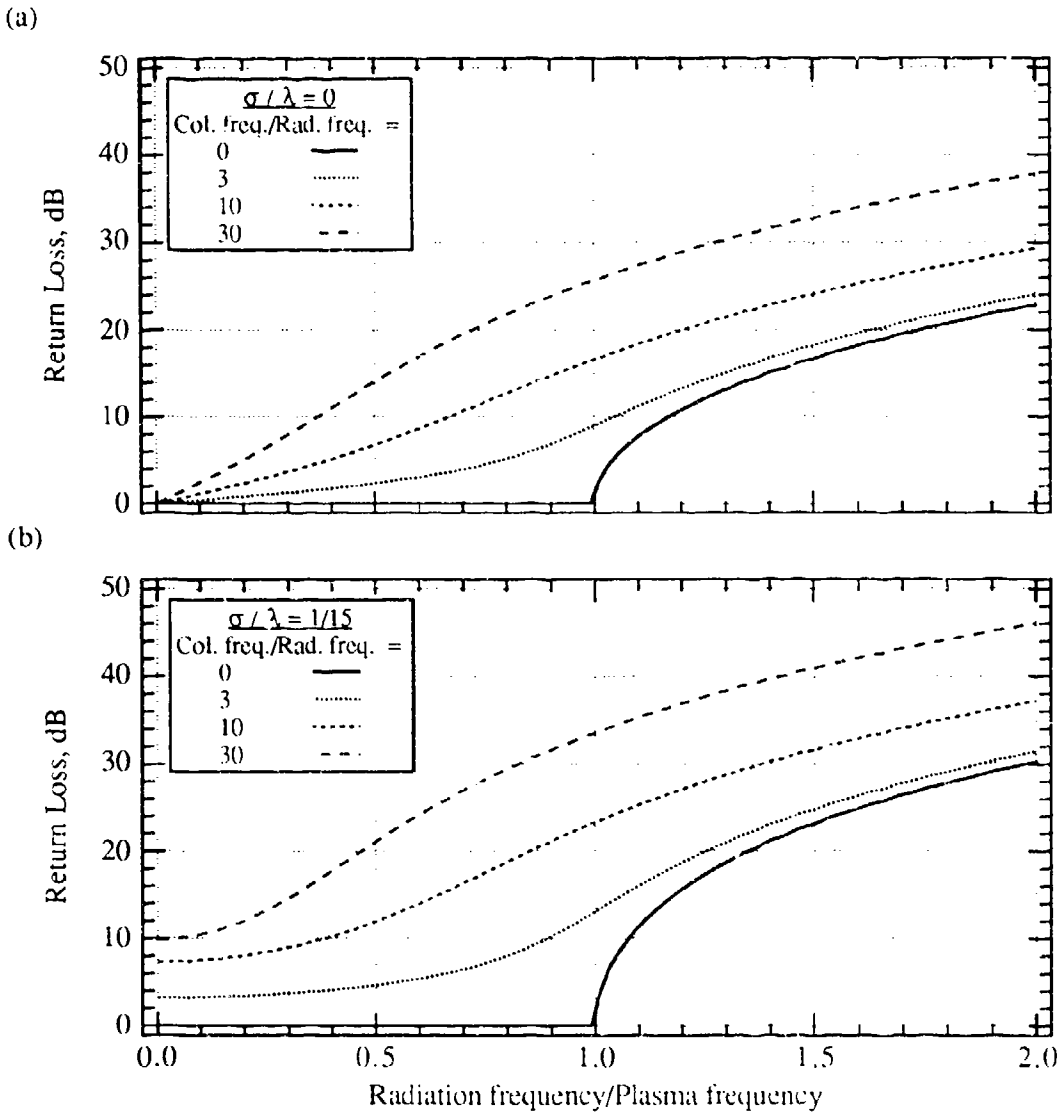

Figure 5 EM-wave reflection from a plasma-vacuum interface for different electron-collision frequencies and EM-wave frequencies. (a) The boundary is infinitely sharp ($\sigma = 0$). (b) The boundary has a slight softening of the density gradient ($\sigma=\lambda/15$). σ is the scale length of the plasma-density gradient.

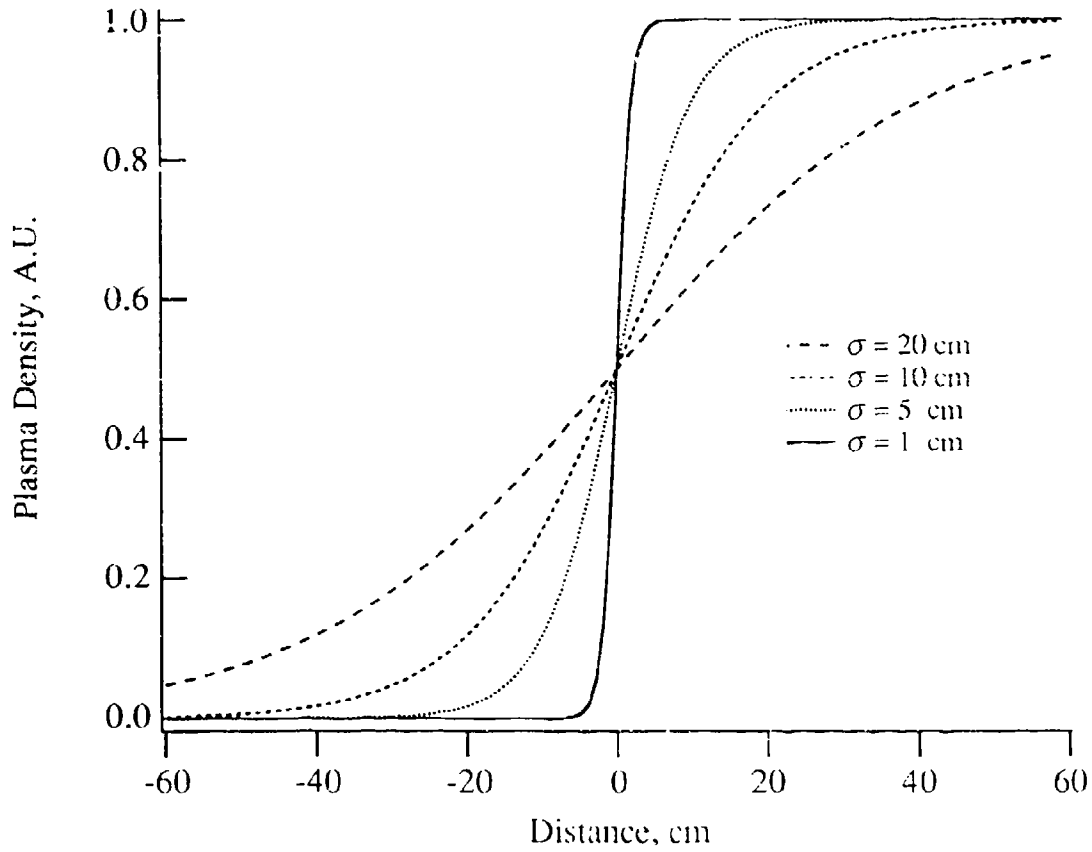

Figure 6 The Epstein profile represents a plasma density profile that can be solved analytically for the partial reflection from the plasma density gradient. The sharpness of the gradient is determined by the characteristic length σ. Several profiles are shown in the figure corresponding to different values of σ. The plasma density goes from 5% to 95% of its peak value with a distance of 6σ.

reflections as long as the plasma's extent is several times larger than σ, the gradient scale factor. Figure 5b plots P_{r2}/P_t vs ω_o/ω_p for various values of ν_c/f_o for $\sigma = (1/15)\lambda_o$, where λ_o is the EM-wave's free-space wavelength. Even though this gradient scale length is small with respect to a wavelength and $\omega_o/\omega_p < 1$, the partially reflected power is still greatly reduced by collisions. It is also important to note that the WKB condition is still satisfied for this particular case.

2.3.3. Total reflection from the plasma-cloaked target

The total reflected EM-wave power is a combination of the power reflected from the vacuum-plasma interface, the partial reflections from the bulk plasma, and the collisionally attenuated waves reflected by the target. An exact calculation of the combination of these reflections is not available analytically because the effects of multiple reflections makes it a very complicated situation. However, an upper limit for the reflected power is computed by summing over the electric fields of the component reflections, calculated from Equations (18), (21) and (23), and assuming that they are all in phase. Figure 7 displays this approximation to the total reflected power versus EM-wave frequency for an EM-wave incident on a target surrounded by an Epstein-profile plasma that extends to $z=-\infty$. Figure 7a shows how the plasma profile's shape affects the attenuation. As seen in the plots, the reflected power is high at the low- and high-frequency ends of the spectrum. The low-frequency end has high reflection due to reflection from the density gradient. Therefore, the reflections at low EM-wave frequencies are more efficiently reduced by the plasma profiles with greater σ values due to the larger size of the plasma relative to the EM wavelength. The wave reflects strongly at high-frequency end because the plasma absorption decreases rapidly as the frequency increases as seen in Figure 2. Figure 7b shows how the reflected power is affected by the electron collision frequency. These calculations agree with those published by Vidmar[3].

2.4. The Plasma-Filled Fabry-Perot Resonator

The effects of multiple reflections from the various interfaces was ignored in the previous section for the sake of simplicity. However, multiple reflections can be very important in a plasma-cloaking system as demonstrated by the data taken on the plasma-filled enclosure of Section 5. In order to understand the complications introduced by multiple interfaces in a plasma-cloaking scenario, this section treats the problem of reflection from a plasma-filled Fabry-Perot resonator.

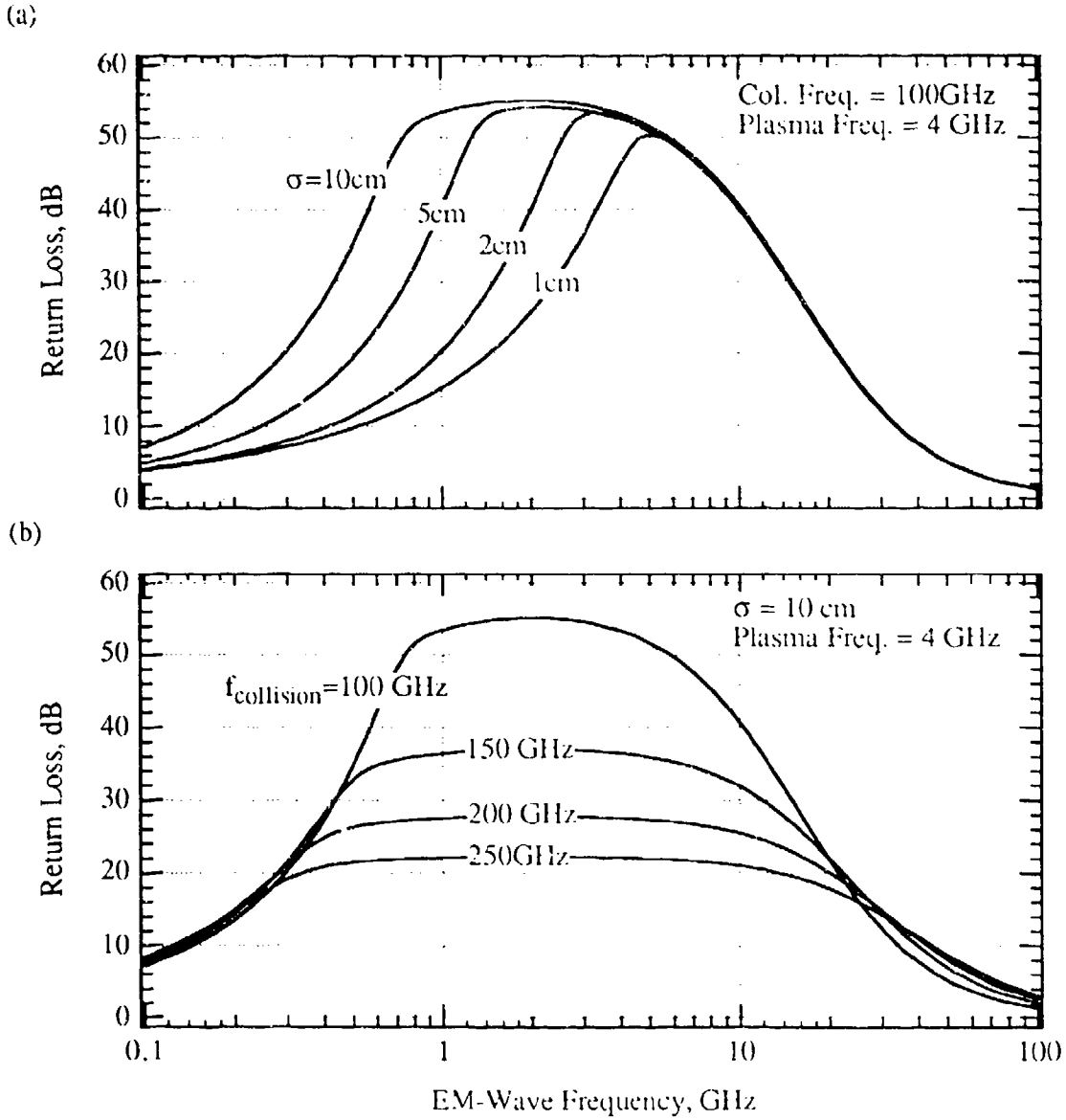

Figure 7 Reduction in reflected power of an EM-wave incident on a target surrounded by 30-cm long, Epstein-profile plasma with a maximum plasma frequency of 4 GHz. Figure 7a displays the reflected power for plasma profiles with σ = 1, 2, 5 and 10 cm and ν_c = 100 GHz. Figure 7b plots the reflection from a σ = 10 cm profile with ν_c = 100, 150 and 200 GHz.

The Fabry-Perot[9] resonator is a pair of partially reflecting parallel plates. In this example, we assume that the space between the plates is filled with a uniform plasma and that the back plate is totally reflective. An EM-wave is incident on the front plate. Some the wave's power is reflected from the front plate while the rest penetrates into the resonator making multiple reflections between the plates. A portion of the wave exits the resonator each time it strikes the front plate. The power reflection coefficient is

$$R = \frac{r^2 + e^{-4k_i L} + 2re^{-2k_i L}\cos(2k_r L)}{1 + r^2 e^{-4k_i L} + 2re^{-2k_i L}\cos(2k_r L)} \tag{24}$$

where r is the reflectivity from the cavity's front interface and the rear interface is assumed to be totally reflective. The plasma's properties are contained within k_i and k_r, the imaginary and real parts of the EM-wave propagation constant in the plasma. For simplicity, the following discussion will ignore the complex character of r and will treat it as a real number.

The effects of multiple reflections are revealed by inspection of Equation (24). For example, if r is equal to the single-pass absorption ($e^{-2k_i L}$) and $2k_r L = \pi, 3\pi, 5\pi, \ldots$ then all the power is absorbed within the cavity and there is no reflection. In contrast, when $2k_r L = 0, 2\pi, 4\pi, \ldots$, the reflected power is 6 dB higher than reflection from the front interface alone. In the limit $e^{-ikL} = 1$, there is no attenuation and 100% of the power is reflected from the cavity. In the opposite extreme where $e^{-2k_i L} \ll r$, the back interface is effectively cloaked and nearly all of the reflected signal is from the front interface.

Figure 8 plots the return loss vs frequency for various ratios of $e^{-2k_i L}/r$. When the ratio is near 1, the return loss has prominent peaks and valleys across the spectrum. As the ratio approaches 0 (See Figure 8a), the reflection from the back interface becomes dominant and the return loss approaches zero. As the ratio becomes large, the back plate is effectively cloaked by the plasma and reflection from the front plate is dominant and constant. The reflection coefficient is then determined by the front plate's reflection coefficient.

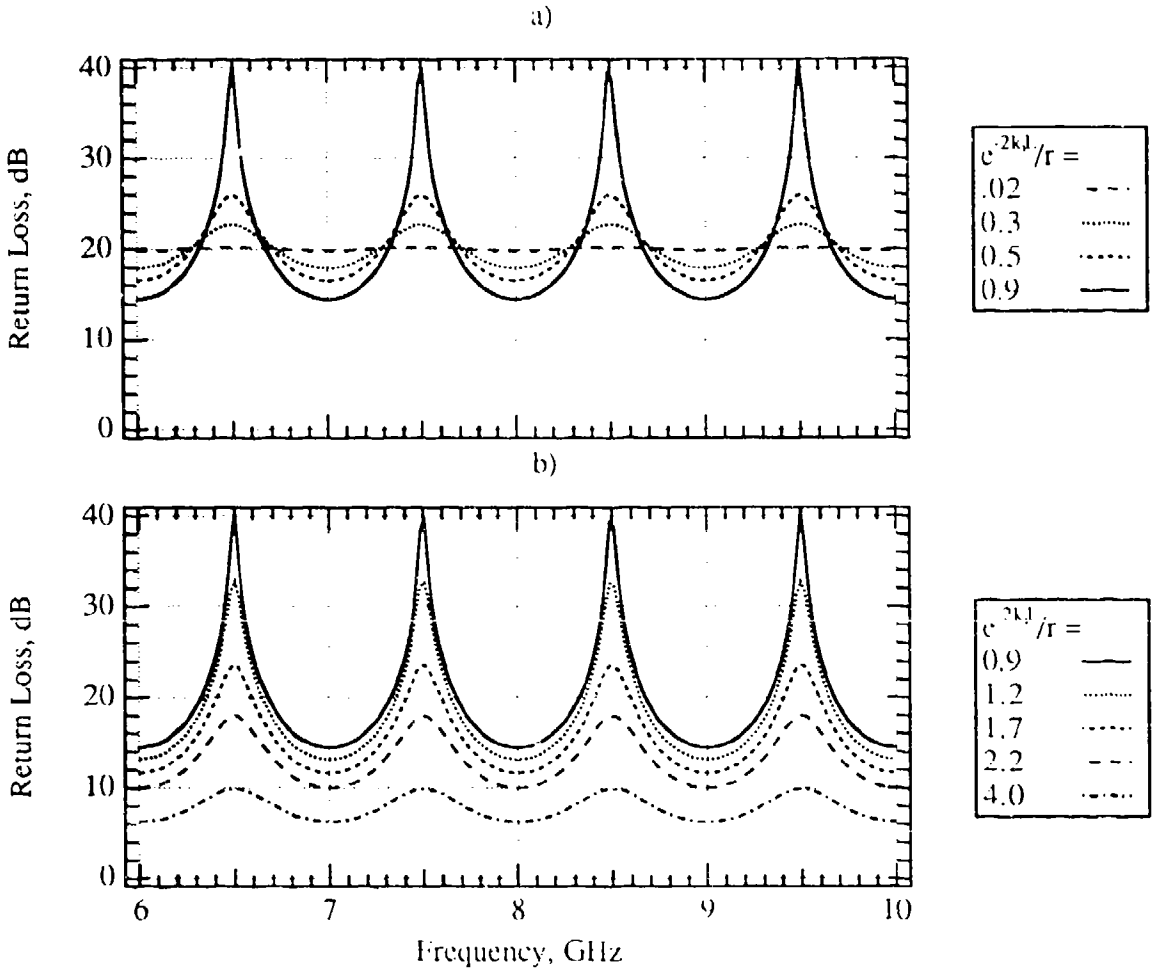

Figure 8 Reflection from a plasma-filled Fabry-Perot resonator. Reflection from a plasma-filled Fabry-Perot resonator can be eliminated completely by appropriate choice of the front interface reflection coefficient (r) and the single pass absorption ($e^{-2k_{1z}}$). The figures plot the return loss of a signal reflected from a resonator with 15-cm plate separation and $r = .1$. In Figure 8a the return loss is plotted for several values of the absorption showing how the reflection is constant at high plasma density and as the density is lowered, the reflection is driven very low as the resonant absorption condition is reached. Figure 8b shows how the return loss behaves as the plasma density continues to decrease. Eventually there is no absorption and total reflection occurs.

3. EXPERIMENTAL DESIGN

In this section we describe the technique used for producing and diagnosing a volumetric plasma to be used in the subsequent experiments on EM-wave absorption in the plasma-filled waveguide and the RCS reduction of the plasma-filled enclosure.

3.1 Plasma-Production Technique

The plasma-production technique is designed to allow independent variation of the plasma density and the electron collision frequency. We used a UV-sustained plasma-generation technology to produce the required plasma densities and plasma-density gradients. Hughes Research Laboratories[10] has previously pioneered this technique for producing spatially controllable, moderate-density plasmas within a high-pressure gas for gas-laser discharges. The technique utilizes UV photoionization of a low-ionization-potential seed gas at relatively low concentration in conjunction with the high-pressure gas. This approach permits us to independently vary the plasma density and the electron collision frequency in order to determine the parameters that optimize EM-wave absorption and refraction. The UV is generated by a high-voltage discharge across an array of spark gaps. The spark-gap array is described in detail in Section 4.

The UV-sustained discharge technique was chosen because it decouples the plasma-production and electron-collision processes, unlike other conventional volume-ionization schemes, such as rf discharges, which involve the dissociation of the background gas to form plasma electrons and ions. We developed the UV-sustained discharge technique at HRL under an earlier DARPA-supported program to produce a volumetrically scalable discharge for exciting high pressure CO_2 lasers[10]. In that program a $CO_2/N_2/He$ mixture at near atmospheric pressure was seeded with a small concentration of a low-ionization-potential organic molecule (tri-n-propylamine) and illuminated with UV radiation from a spark-gap array. Photoionized electron densities $>10^{12}$ cm^{-3} were produced throughout an atmospheric-pressure background-gas volume of about 20 liters.

In our present experiments, we found that a seed/background-gas mixture of Ar/He provides satisfactory plasma-production rates. This gas mixture greatly simplifies the experimental apparatus since other candidate seed gases would require special handling because of their toxicity. The UV-photoionization cross-sections[11] as functions of photon energy for several inert gases are shown in Figure 9. Photons with energies between 21 and 16 eV penetrate the high-pressure He gas and ionize the Ar seed gas. We have found

empirically that UV emission from the spark gaps described in Section 4 has sufficient intensity in this spectral regime to induce satisfactory ionization. We can estimate the size of the ionized volume. The UV radiation intensity will obey an exponential decay law

$$I(x) = I_o e^{-x/\zeta} \quad , \tag{25}$$

where $I(x)$ is the intensity at position x, I_o is the intensity at the spark gap at $x=0$, and $\zeta = (760/\mu P_{Ar})$, is the UV absorption distance, where μ is the absorption coefficient in cm^{-1} shown in Figure 9, and P_{Ar} is the argon seed-gas pressure in Torr. The plasma density is then proportional to derivative of $I(x)$ with respect to x,

$$n_e \propto -\frac{dI(x)}{dx} = \frac{I_o}{\zeta} e^{-x/\zeta} \quad . \tag{26}$$

In our experiments, we typically used Argon pressures from 100 to 400 mTorr; if we use $\mu = 600\ cm^{-1}$ we find that ζ varies from 12.7 to 3.2 cm.

It was not possible for us to estimate the plasma density prior to doing the experiments as there were several unknown factors involved in the calculation including the spark-gap's UV spectrum and efficiency and the impurity concentration in the gas mixture. In practice, empirical observation of the plasma properties were the fastest way to optimize the plasma generator. However, we were able to estimate the optimum argon pressure based on manipulation of Equation (26). Simple analysis yields the condition for maximum plasma density at a fixed point x, to occur when $\zeta=x$. Therefore, the optimum pressure is $P_{Ar}=760\ Torr/x\mu$. In the plasma-filled waveguide experiments (See Section 4), the distance from the spark gaps to the waveguide axis was 10 cm, thus the optimum argon pressure is predicted to lie within the range from 100 to 200 mTorr depending on the value of μ used.

During the experimental measurements, questions were raised as to whether the plasma was indeed being formed through the UV-photoionization process or if it was created within the spark gap and propagated outward to fill the rest of the vacuum chamber. An important piece of data used to resolve this point was the relative timing between the spark-gap current pulse and the EM wave absorption (See Figures 20 and 30) in the plasma-filled waveguide. The data showed that the initiation of the current pulse and the onset of the absorption were simultaneous. This ruled out any possibility of plasma propagation from the spark gaps being the plasma source, since it would have taken nearly 100 μsec after the current pulse for any absorption to occur; based on the fact that a plasma in the pressures used would propagate at the speed of sound (~100 m/sec).

Further verification of the UV-photoionization method was given by the empirical agreement of absorption vs argon pressure with the calculations based on Equation (26).

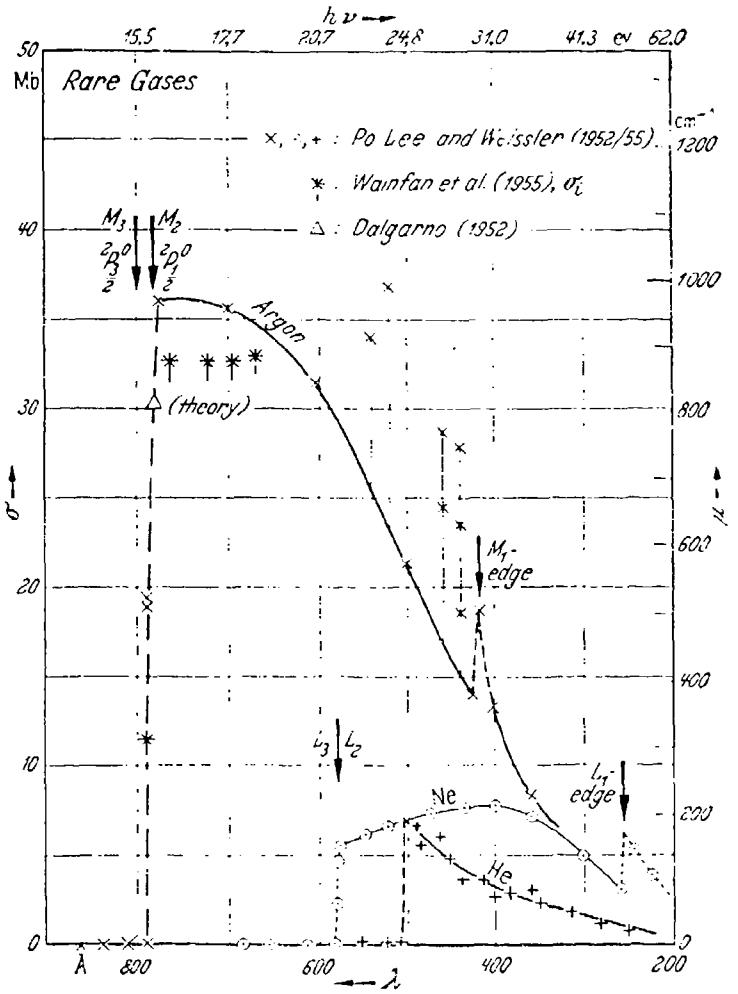

Figure 9 Photoionization cross sections for He, Ne, and Ar[11].

As the argon pressure was raised from zero, the absorption increased to a maximum near 170 mTorr and then steadily decreased thus indicating that the plasma density in the waveguide had followed a similar course. The observed behavior was in good agreement with the predictions.

3.1.1 Plasma formation and energy efficiency

An ideal plasma cloaking system would create a CW plasma for a small energy cost. The methods described in this paper are very primitive and were developed to merely demonstrate the feasibility of plasma cloaking. In order to engineer a viable plasma-cloaking system for an airborne platform, more efficient means must be used to create the plasma. Gas purity is absolutely imperative for an efficient system. As an illustration of the effects impurities have on a plasma, Figure 10 displays the plasma lifetimes for helium as a function of gas purity as computed by Vidmar[3]. It shows that an increase of several orders of magnitude can be achieved with a pure gas. The resultant energy requirements are calculated from the rate equations.

$$P = k\, n_e^2\, E_i\, \eta^{-1} \tag{27}$$

where P is the power per unit volume necessary to maintain a plasma at constant density n_e in a gas with an ionization potential E_i and a recombination rate k. The plasma lifetime is related to the recombination rate by $\tau = 1/k\, n_e$. Table 1 lists the recombination rates and ionization potentials for several gases along with the power to sustain a plasma as calculated from Equation (27).

Another way to increase efficiency is to use a gas which is readily ionized but has a low intrinsic recombination rate. The noble gases are particularly attractive because of their low recombination rates and their low affinity for free electrons. However, their ionization potentials lie at 10 eV or higher. If it were possible to find other materials with lower ionization potentials that still have low recombination rates and low radical coefficients, then efficiency could be driven even higher. Possibilities exist for exotic organic vapors such as Tetrakis-(dimethylamino)ethylene (TMAE), an organic material with $E_{ion} \sim 6$ eV. On the down side, such materials would break down in any high-voltage discharge being used to create the plasma, therefore a flowing gas system is necessary in order to maintain gas purity. The organic materials are also hard to handle because of their toxic properties.

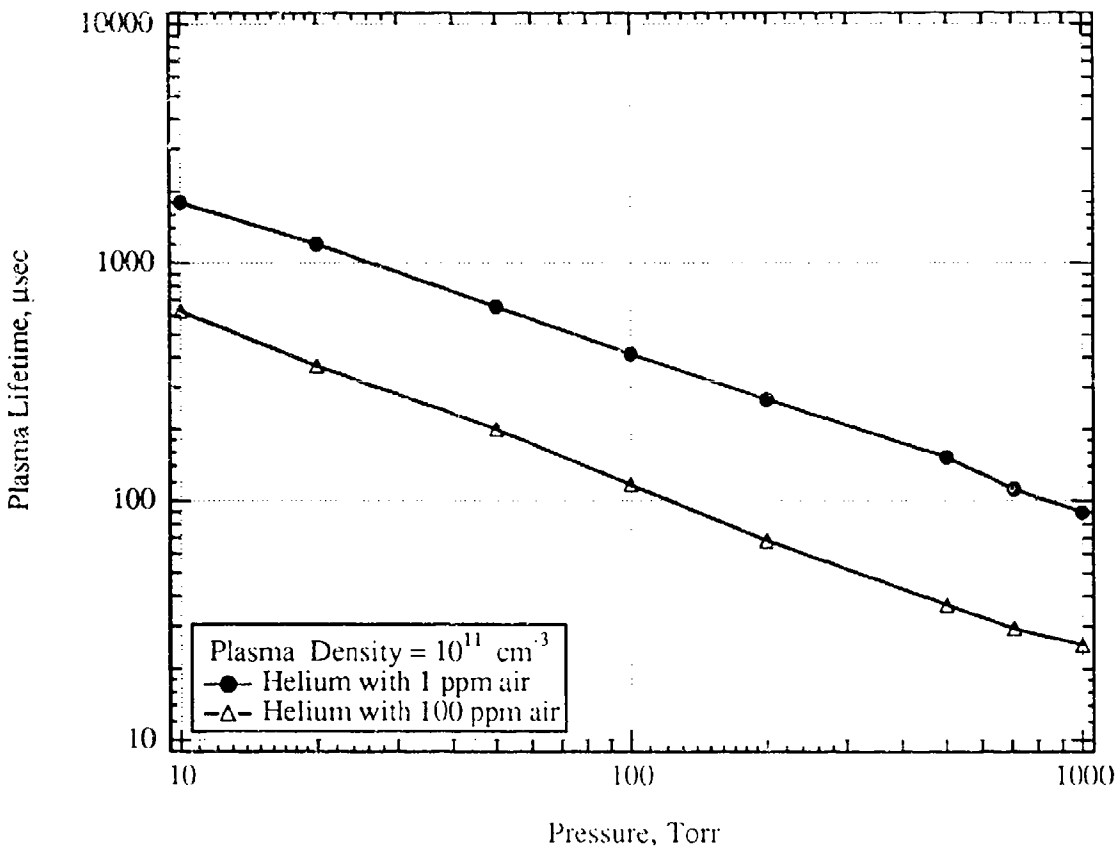

Figure 10 Plasma lifetime vs gas purity. A plasma will recombine at a much slower rate if the impurity level is kept low as demonstrated in the graph where the lifetime of a 10^{11} cm^{-3} Helium plasma is plotted vs gas pressure for two different impurity levels. In our experiments, the lifetime was observed to be ~6 μsec thus indicating that our impurity level was much higher than 100 ppm.

Gas	k (cm^3/sec)	E_i (eV)	P (Watts) $n_e = 10^{11}$ cm^{-3}	P (Watts) $n_e = 10^{12}$ cm^{-3}
Helium*	1.0×10^{-8}	24.5	20	1960
Helium w/ 1 ppm Air	2.4×10^{-8}†	24.5	47	4704
Helium w/ 100 ppm Air	8.3×10^{-8}†	24.5	162	16268
Neon*	1.8×10^{-7}	21.6	311	31104
Argon*	9.1×10^{-7}	15.8	1150	115024
Krypton*	1.6×10^{-6}	14.0	1792	179200
Xenon*	2.7×10^{-6}	12.1	2613	261360
TMAE††	$\sim 3.0 \times 10^{-6}$	~ 6.	1440	144000

* Rates based on two-body dissociation

† As calculated from Figure 10 and Equation (27) for P=100 Torr

†† Estimated values for k and E_i

Table 1. Plasma Power Requirements are computed according to Equation (27) for maintaining uniform plasma density in a volume of 5000 cm^3 with a 10% efficient plasma ionization source. Two-body dissociative recombination is assumed to be dominant except in the case of Helium with impurities which is assumed to be at a pressure of 100 Torr.

3.2 Vacuum System

A glass-"T" vacuum system was assembled for the plasma-filled waveguide experiments of Phase I of this program. A mechanical vacuum pump is used to evacuate the glass-"T" to a base pressure of 5 mTorr. A valve between the pump and the glass-"T" is used to isolate the chamber from the pump during the experiments. A DV-6M Hasting gauge is used to monitor pressures in the 1 to 1000 mTorr range (seed gas), and a Model-760 Hasting gauge and a Bourdon gauge cover the 1 to 760-Torr range. Independent gas-feed systems are used to control the seed-gas and background-gas pressures. Each gas-feed system consists of a gas bottle, a high-pressure regulator, a purge line, a leak valve and a shutoff valve. To maintain a specified seed/background gas mixture, we evacuate the chamber, and then close the vacuum valve to isolate the chamber from the pump. We first leak in the seed gas to the desired pressure (monitored using the model DV-6M gauge), and then introduce the higher-pressure background gas (monitored using the model 760 gauge). Since the Ar/He gas mixture does not decompose during the photoionization process, a flowing-gas system is not required.

The vacuum vessel utilized for the plasma-filled ceramic enclosure experiments was the ceramic enclosure itself. A metal flange was fitted to its back end with an O-ring seal and all of the vacuum valves and gas-handling components were tied into the enclosure via the back flange. Gas-transfer operations were nearly identical to those used with the glass-"T" vacuum system described above.

3.3 High-Voltage Modulator

The high-voltage modulator assembled for this program is shown in Figure 11 is basically a simple capacitor discharge circuit. A single GL7703 ignitron switch is used to close the high-voltage, high-current capacitor discharge circuit. A 15-kV power supply pre-charges each capacitor through a 100-kΩ resistor. The capacitor charging path is completed by a 2-kΩ resistor. When the GL7703 ignitron is triggered, the high-voltage immediately appears across the spark-gap array. If the voltage exceeds the breakdown voltage (measured to be ~1.5 kV), the spark gaps fire and the capacitors are discharged through the gaps. High-voltage probes and current transformers are used to monitor the pulsed voltages and currents, respectively. After initiating the arc, the current decreases with a characteristic R'C decay time constant, where R' is the sum of the series resistance (10 ohms) and the arc resistance. Since the voltage drop across the spark-gap is very low after breakdown is initiated, the current through the gaps, and hence the intensity of the UV emission, is controlled by varying the capacitor charge voltage and the series resistance. Special feedthroughs were fabricated to couple the high-voltage into the vacuum system. The feedthroughs consist of 20-kV bushings soldered to modified Swagelock O-seal fittings. Twenty-kilovolt high-voltage (HV) wire is soldered to the high-voltage bushing to form part of the vacuum seal. The HV wire is then routed to the different spark-gap elements. This system has provided reliable operation up to a maximum test voltage of 15 kV with He-gas pressures from 150 to 500 Torr.

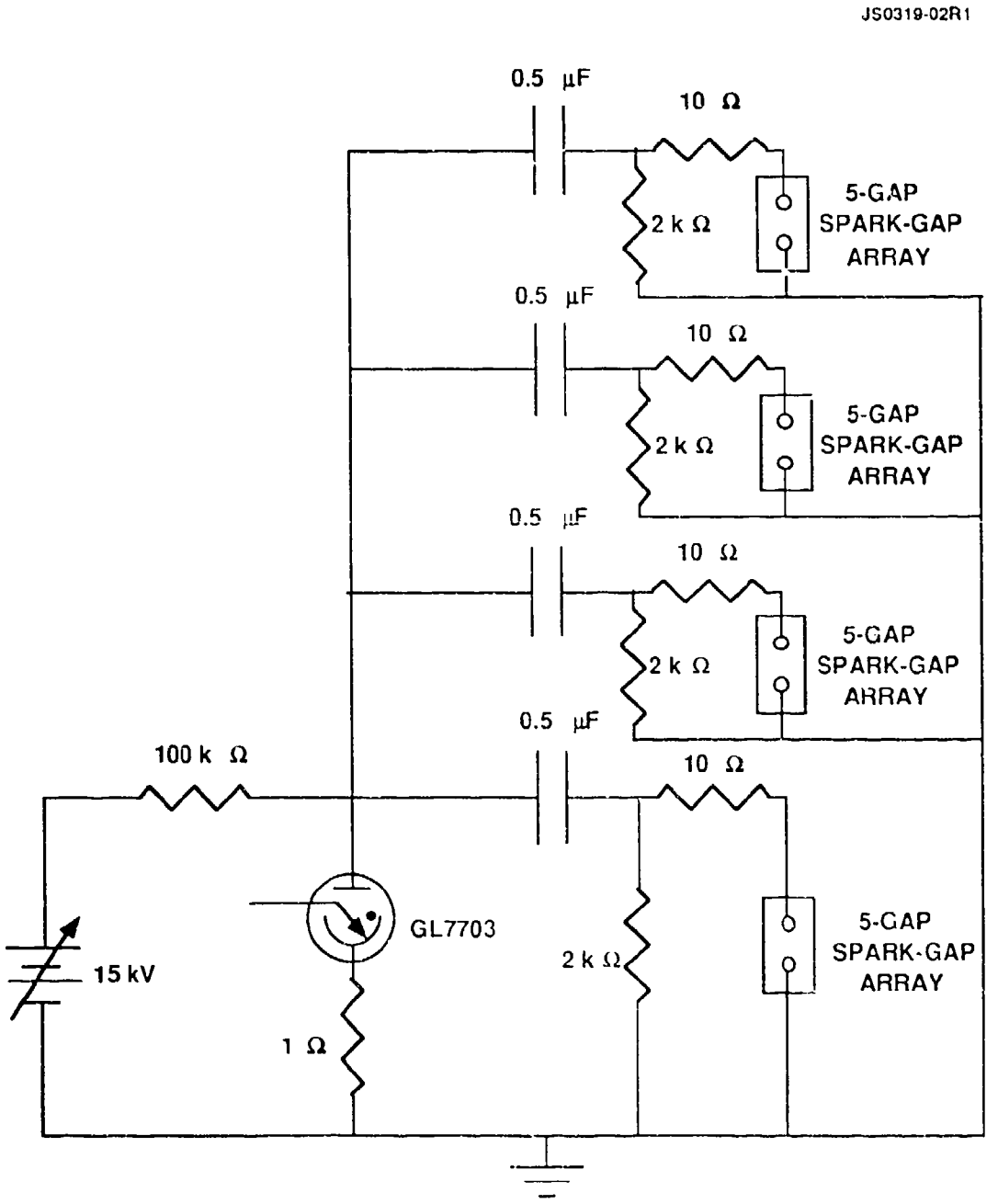

Figure 11 High-voltage spark-gap modulator.

4. PLASMA-FILLED WAVEGUIDE EXPERIMENTS

In this section we describe our experiments investigating EM-wave absorption in a plasma-loaded section of C-band waveguide beginning with a description of the apparatus, in particular the spark-gap array and the slotted waveguide assembly. We then proceed to discuss the plasma density measurements and the EM-wave propagation experiments. Our results are then compared to theory and shown to be in good agreement.

4.1. Critical Design Components

4.1.1. Spark-gap array

For preliminary experiments, a three-gap spark array was designed by carefully considering high-voltage breakdown in a 1 to 760 Torr gaseous environment[12-14]. The main requirement is that the breakdown occurs between the electrodes and not the electrode supports. Based on the results of this design study, we used 0.16-cm-diameter tungsten electrodes sharpened to a point and mounted in 0.64-cm-diameter polished stainless-steel electrode holders (Tantulum electrodes worked equally well except that they had a higher erosion rate). The modulator described in Section 3.3 was used to test the preliminary spark-gap array at pressures ranging from 5 mTorr to 760 Torr. We tested the array in one, two, and three-gap configurations to determine the scaling of the minimum breakdown voltage at different pressures with the number of gaps and the tungsten-electrode spacing. We found that a gap spacing of 0.64 cm provides reliable operation from 150- to 760-Torr He-gas pressure with a minimum breakdown voltage of about 3 kV for a three-gap array. Operation at lower pressures was extremely difficult due to glow discharges between the high-voltage-electrode support and the grounded waveguide. There were also problems with Paschen breakdown inside the high-voltage feedthroughs at the lower pressures.

Using these data we designed four arrays with five spark gaps per array. Each five-gap array was found to have a breakdown voltage of 4 kV. Figure 12 shows the spark-gap arrays mounted on the slotted waveguide, which is described in the next subsection.

4.1.2. Slotted waveguide

The slotted waveguide is the key element in the EM-wave transmission system; it solves the problem of allowing plasma to be injected into the waveguide without disturbing the waveguide's transmission characteristics. We performed theoretical calculations and

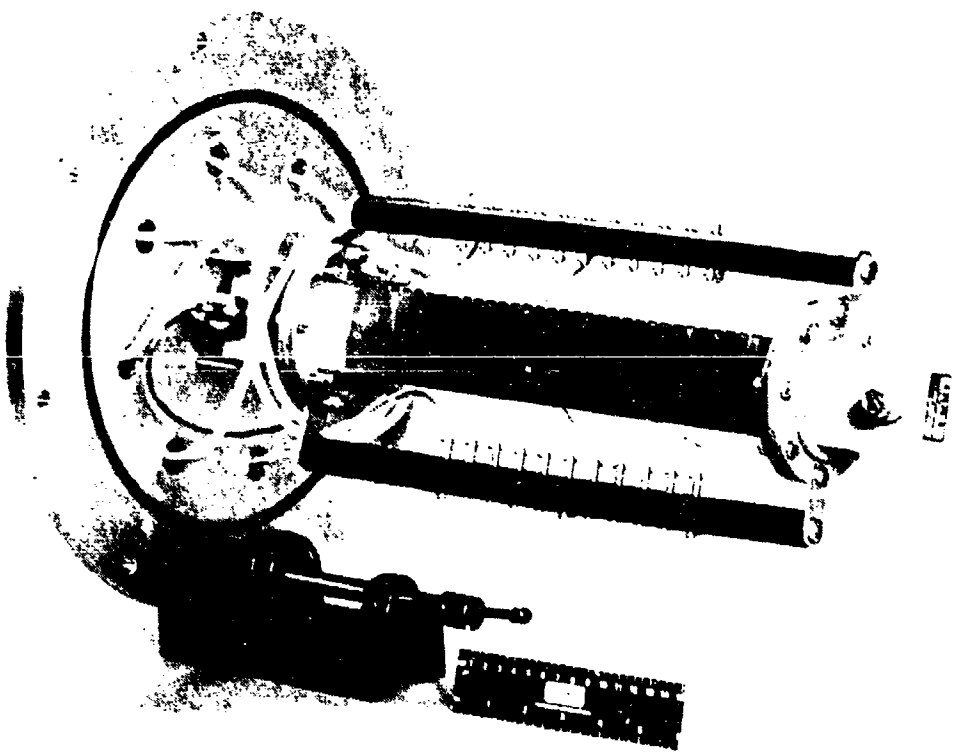

Figure 12 Slotted waveguide and spark-gap array mounted on vacuum flange.

several experiments to validate the concept prior to fabricating the full-scale slotted waveguide. Our calculations[15, 16] indicated that a C-band (WR187) waveguide with 75% to 80% sidewall transparency will have negligible perturbation on the transmitted wave. Using the calculations as a guide, we fabricated a five-slot, 75%-transparent section of C-band rectangular waveguide (slot width = .64 cm). The slots are cut into the short walls on the waveguide because the electric field of the fundamental mode vanishes at these walls. Therefore, there are no wall currents that can be interrupted by the walls. The slots' effect on transmission properties was examined by measuring the waveguide insertion loss using a scalar network analyzer; the slots were found to have virtually no effect. Less than 0.1-dB change in the waveguide's transmission loss was measured.

Encouraged by the test piece's high performance, we then fabricated the 30-cm-long section of C-band waveguide with 75% wall transparency shown in Figure 13. The measured insertion loss is shown in Figure 14, where the in-band characteristics of the coax-to-waveguide adapters and coaxial cables have been subtracted out. The insertion loss is less than 0.2 dB over the C-band operating frequencies of 4 to 6 GHz. This insertion loss is much less than the EM-wave attenuation expected in the cloaking experiments therefore we expect to accurately measure the effects of plasma on the wave propagation in the waveguide without having to worry about the effects of the imperfect walls.

4.2. Plasma Density Measurement

We installed a cylindrical Langmuir probe to measure the plasma-density profile We sampled the axial plasma density by removing one coax-to-waveguide adapter and inserting the probe into the waveguide. The probe was biased at +45 V to collect electron current, which provides a relative measure of the local electron density. Two plasma profiles are shown in Figure 15. One profile was recorded when 700 A was discharged through 19 spark gaps. The second profile resulted when 680 A was discharged through only 10 spark gaps (one five-gap array on each side of the slotted waveguide). From the profile measured when the 19 gaps were fired, we find that the plasma extends for about 22 cm (half-maximum points on the electron-current profile) within the waveguide and has a gentle gradient at either end. At this point, we have not yet assigned an absolute plasma density to the profiles in Figure 15 because we have found that the Langmuir probe theory developed for highly collisional plasmas is computation intensive. However, we have applied an empirical technique based the data from the plasma-filled waveguide's absorption experiments (See Section 4.3) and applied a non-linear curve fit to determine the plasma density. The curve fit is based on the theory of Section 2 and we assumed uniform

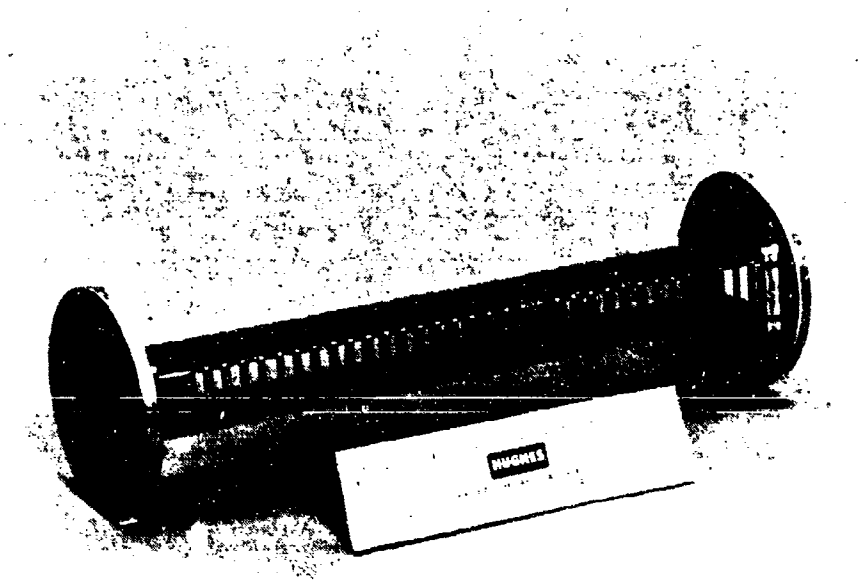

Figure 13 Slotted, 30-cm-long WR187 waveguide section.

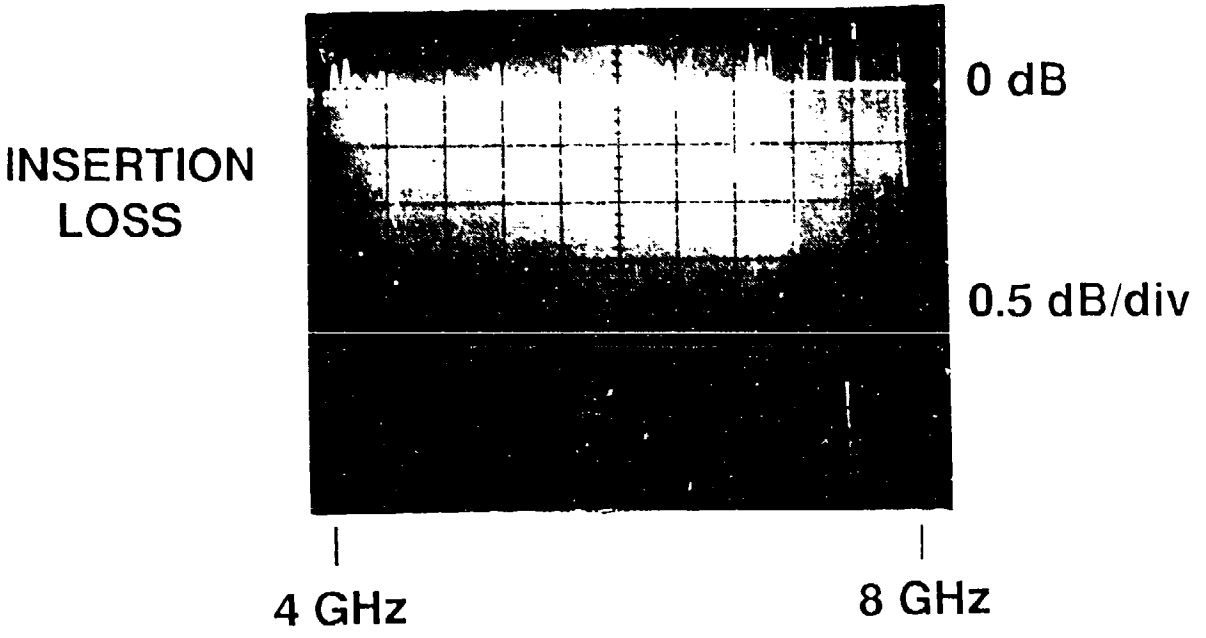

Figure 14 Slotted-waveguide insertion loss measured using scalar network analyzer. The insertion loss is less than 0.3 dB when system is operated in the fundamental TE_{10} mode (4 to 6 GHz).

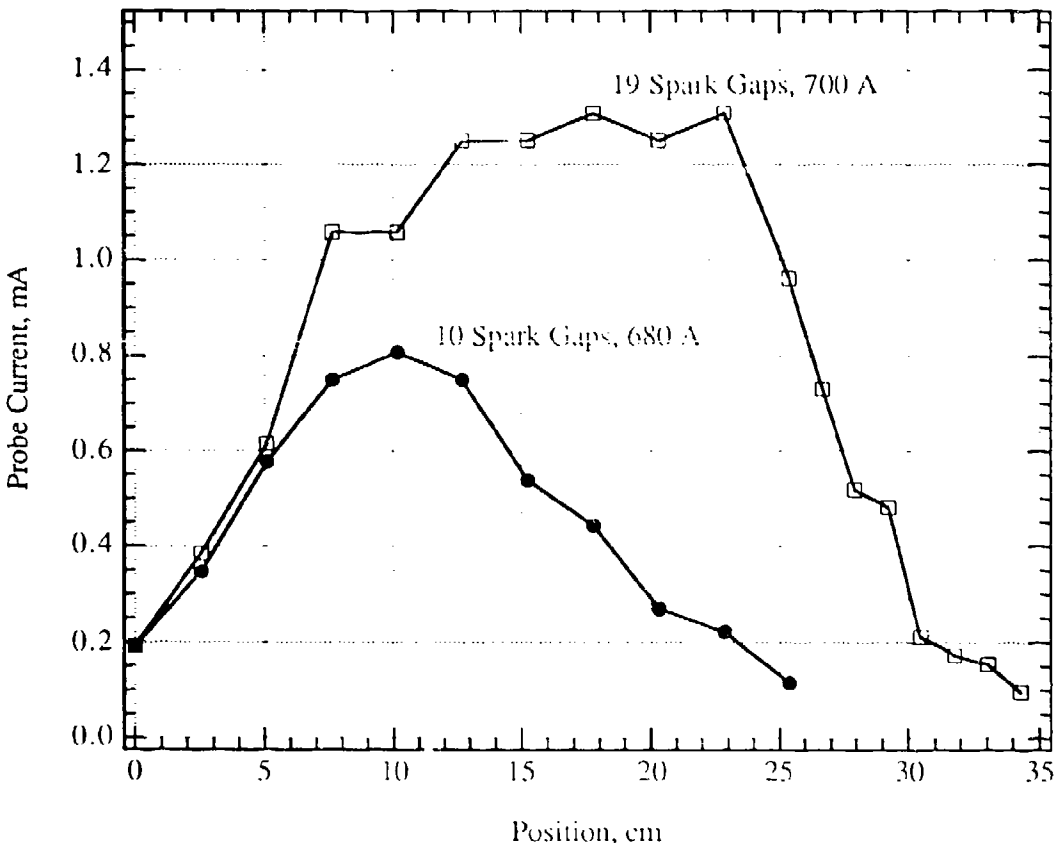

Figure 15 Axial plasma-density profile within the slotted waveguide. The electron current collected by biasing the probe to +45 V is approximately proportional to the electron density.

plasma density across the waveguide's cross section. As shown in Figure 16, the plasma density scales proportional to the square of the spark-gap current. A corollary is that the corresponding plasma frequency scales linearly and a curve is fit to the data points based on this simple dependence. The linear behavior is easy to demonstrate analytically if we assume that the spark-gap impedance is constant and the power that goes into the plasma generation is proportional to the power dissipated across the arc; then $n_e \propto P_{arc} = I_{arc}^2 R_{arc}$ and $f_p \propto I_{arc}$. On the other hand, we can expect complications due to the following uncertainties; the spark gap's UV spectrum as a function of current , the gap's radiation efficiency, the stability of the spark-gap impedance and the modeling of the true plasma profile. As seen in the curve fit of Figure 16, the complications do not introduce serious aberrations.

We also used the Langmuir probe to measure the relative plasma density as a function of argon seed-gas pressure in order to verify the optimum value as predicted by the UV-photoionization analysis of Section 3.1. The electron probe current was monitored as the seed-gas partial pressure was increased from 0 to 1 Torr by holding the probe at a fixed +45 V bias. The helium pressure was also varied from 200 to 400 Torr. The probe current peaked at argon pressures near 150 mTorr corresponding to an e-folding UV-absorption length of about $\zeta \sim 10$ cm, thus verifying the calculations of Section 3.1 that showed that the argon/helium gas mixture was suitable for our absorption experiments.

4.3. Absorption in the Plasma-Filled Waveguide

In this section we describe absorption experiments demonstrating a maximum of 63 dB attenuation for a 4-GHz EM wave propagated through the plasma-loaded waveguide. These experiments employed the four, five-gap spark arrays and the slotted C-band waveguide shown in Figure 17, the microwave transmission systems shown in Figures 18 and 19, and the spark-gap modulator shown in Figure 11.

We assembled the EM-wave transmission system shown in Figure 18. The pulse generator gates the microwave signal source on for approximately 50 μs. The signal is then amplified to approximately 1 W. An isolator prevents power reflected from the amplifier input from returning to the signal source. The output from the amplifier is routed through a circulator to isolate the amplifier from the plasma-loaded waveguide. Directional couplers and diode detectors are used to measure the power incident on, reflected from, and transmitted through the plasma-loaded waveguide. Hermetically sealed SMA feedthroughs are used to route the microwaves into the vacuum chamber. Standard WR187 coax-to-waveguide adapters match the coax cables to the plasma loaded waveguide. This transmis-

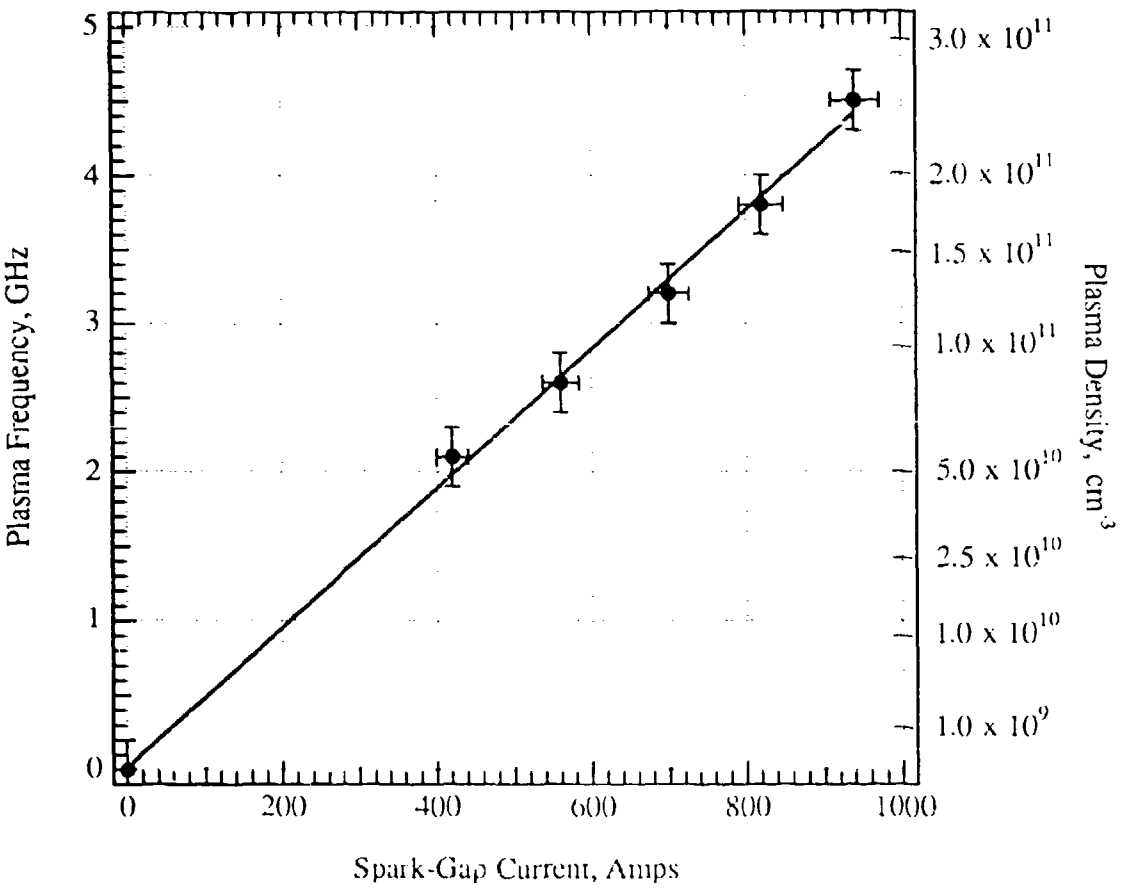

Figure 16 Plasma-frequency scaling with spark-gap current.

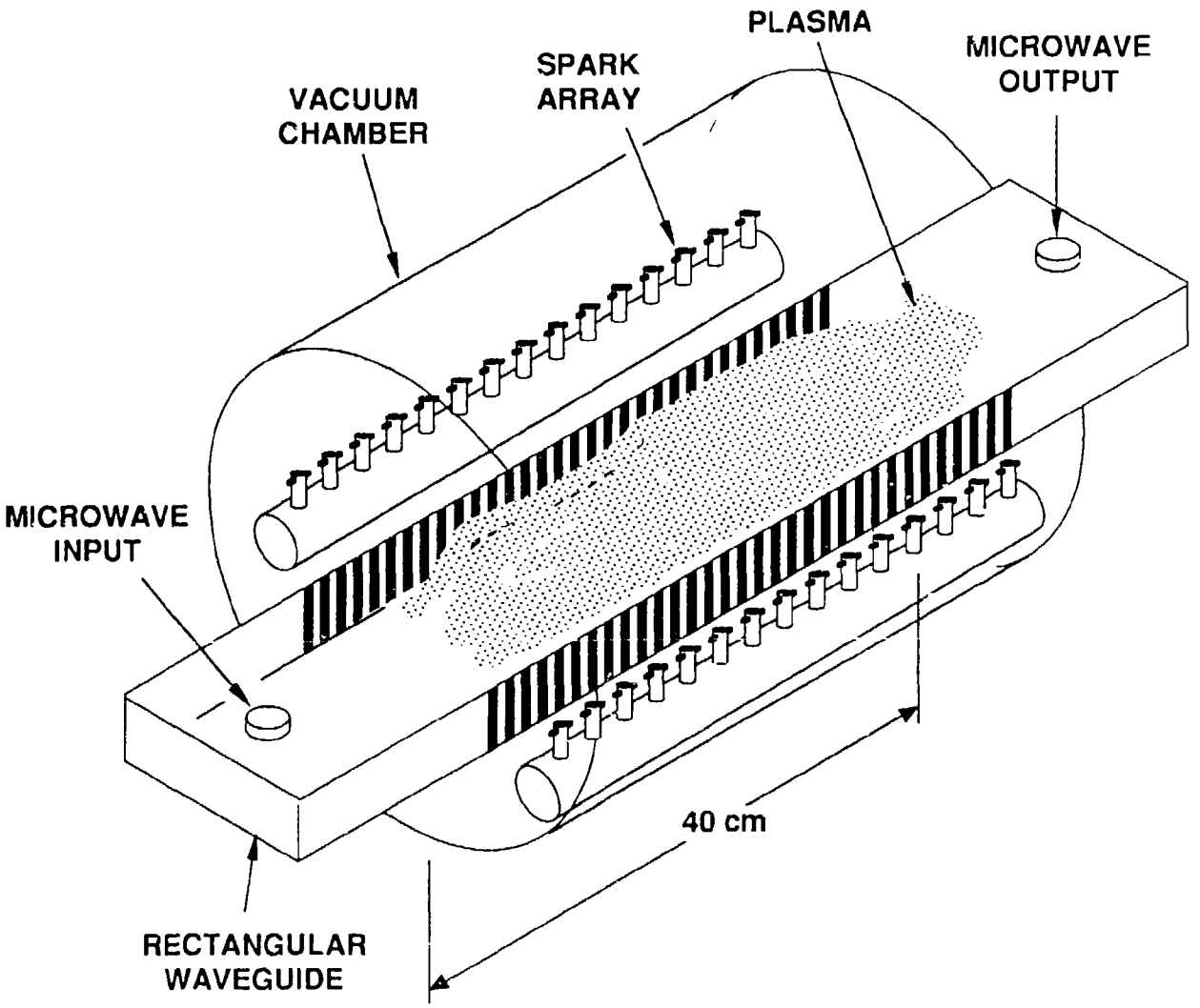

Figure 17 Rectangular waveguide and spark-gap array used in the plasma-filled waveguide experiments. The spark gaps, mounted parallel to the waveguide axis, produce UV radiation that penetrates the waveguide through slots in the sidewalls. The UV ionizes an Argon-Helium gas mixture inside the waveguide to density as high as 10^{12} cm^{-3}

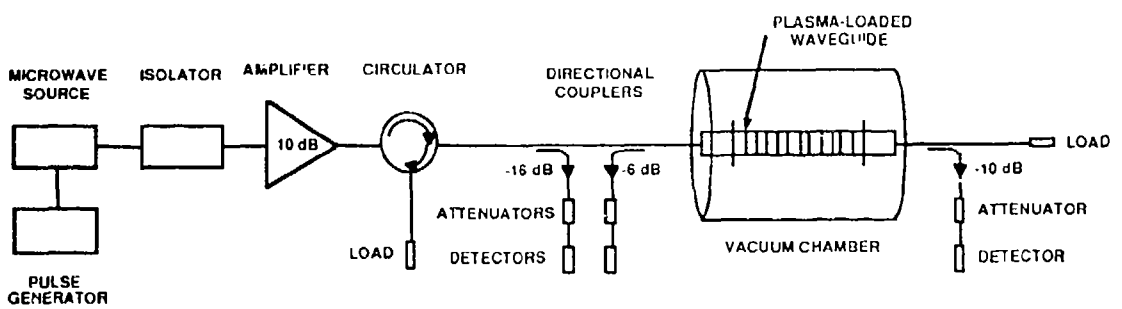

Figure 18 Electromagnetic-wave transmission system using diode detectors.

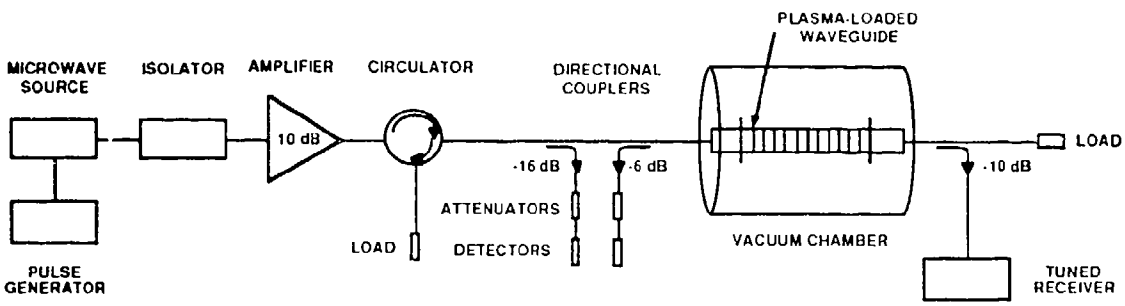

Figure 19 Electromagnetic-wave transmission system using a spectrum analyzer as a tuned receiver. The tuned receiver increases the dynamic range to about 70 dB.

sion system had about 15 dB of dynamic range. We increased the dynamic range to more than 70 dB by installing the 10-dB amplifier and by replacing the diode detectors with a spectrum analyzer employed as a tuned receiver as shown in Figure 19. To eliminate electromagnetic interference (EMI) produced by the short-duration, high-current spark-gap pulses, and ground-loops, we installed the signal source, amplifier, diode detectors, and tuned receiver inside an EMI-shielded screen room. This eliminated all ground loops and EMI effects.

The timing scenario for the experiment is displayed in Figure 20. The microwave source is gated on by the pulse generator as described above. The turn-on time is chosen to be about 10 μs before the spark gaps are triggered. This enables us to calibrate microwave transmission losses by comparing the power transmitted through the system with the plasma OFF and then ON. In the ideal case of VSWR = 1, there is no reflected power when the plasma is OFF because the 50-ohm load absorbs all the incident power, and there are no reflections from the various waveguide and coaxial components. (VSWR stands for variable standing wave ratio; it is a measure of how much power is reflected from a microwave transmission line system or various components.) However, the reflected power actually includes the signals reflected from connectors, cables, and adapters in the transmission system. In fact, we have found that a major contribution to the reflected power is from the coax-to-waveguide adapters, which the manufactures quotes as having a VSWR of ≤1.25. This specifies an ultimate sensitivity limit of 19 dB for the reflected power relative to the input signal. With the plasma on, the measured reflected power can increase or decrease depending on the standing-wave pattern at the directional coupler. This standing-wave pattern is created by the multiple reflections of the microwave signal from the various coaxial and waveguide components on the input side of the plasma-loaded waveguide section. This is because the standing-wave pattern changes when the reflected power originating from the components on the output side of the plasma-loaded waveguide section is attenuated by the plasma.

We performed the cloaking demonstration shown in Figure 21 to unambiguously demonstrate that the microwave power is not reflected by the plasma. The 50-ohm load normally used to terminate the transmission system is now replaced by a short. This reflects all the microwave power that reaches the short back toward the plasma loaded waveguide. Before the plasma is pulsed, the transmitted and reflected powers are roughly equal. When the plasma is triggered, both the transmitted and reflected power decrease to very low levels thus demonstrating that the short at the end of the transmission line was effectively cloaked by the plasma.

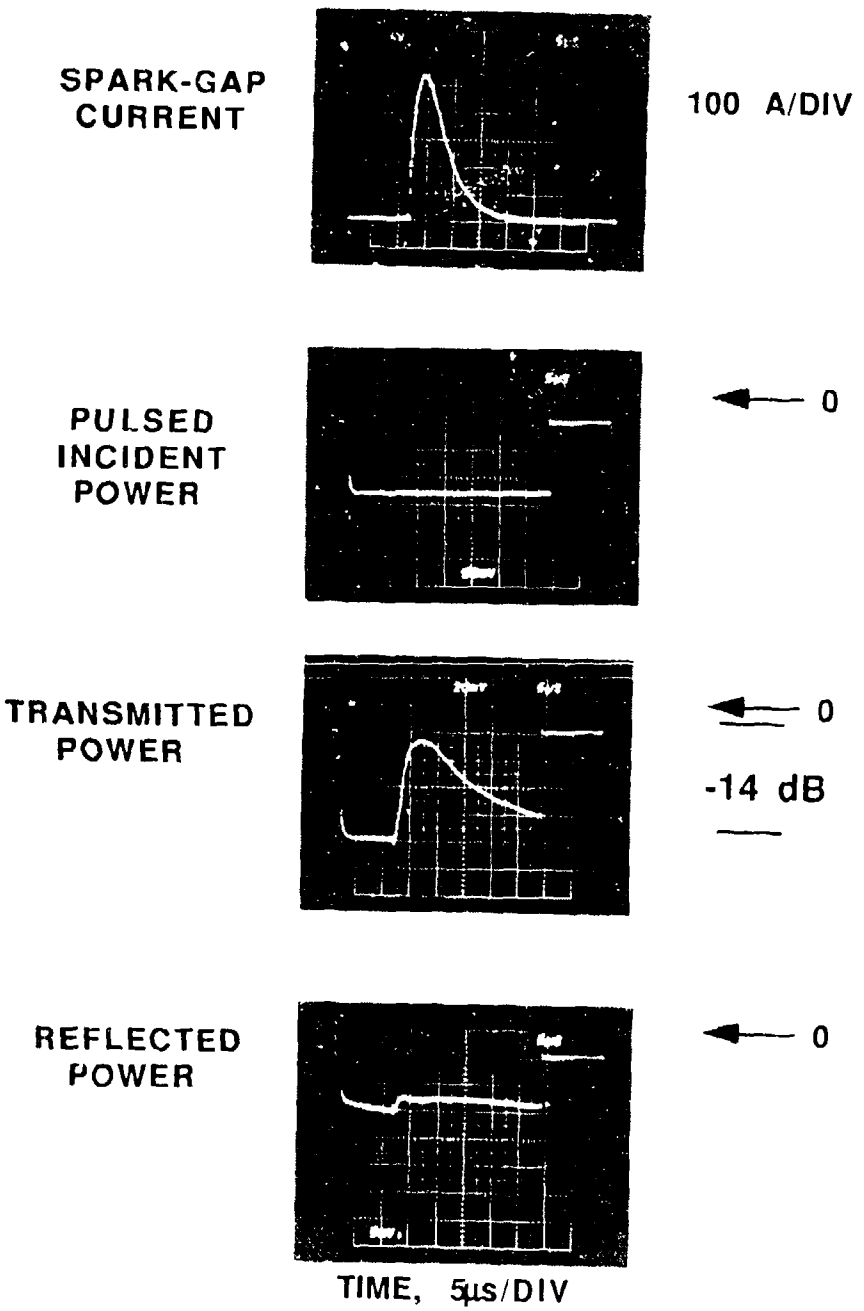

Figure 20 Timing scenario for plasma-filled waveguide experiment. The microwaves are pulsed about 10 μs before the plasma is triggered.

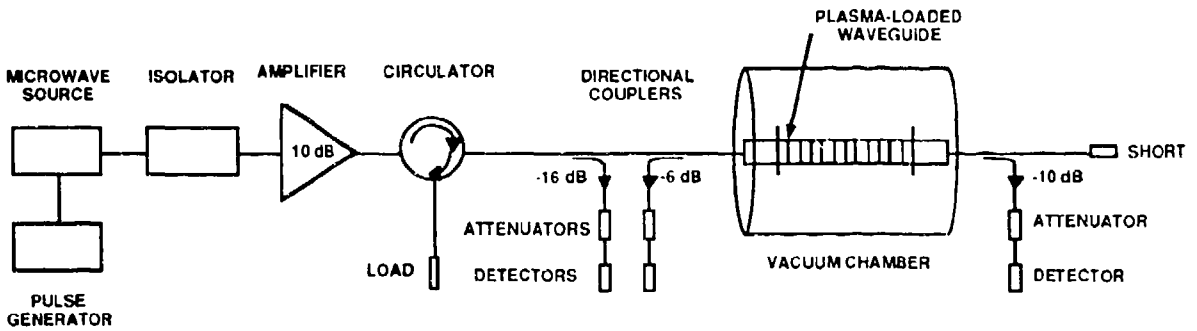

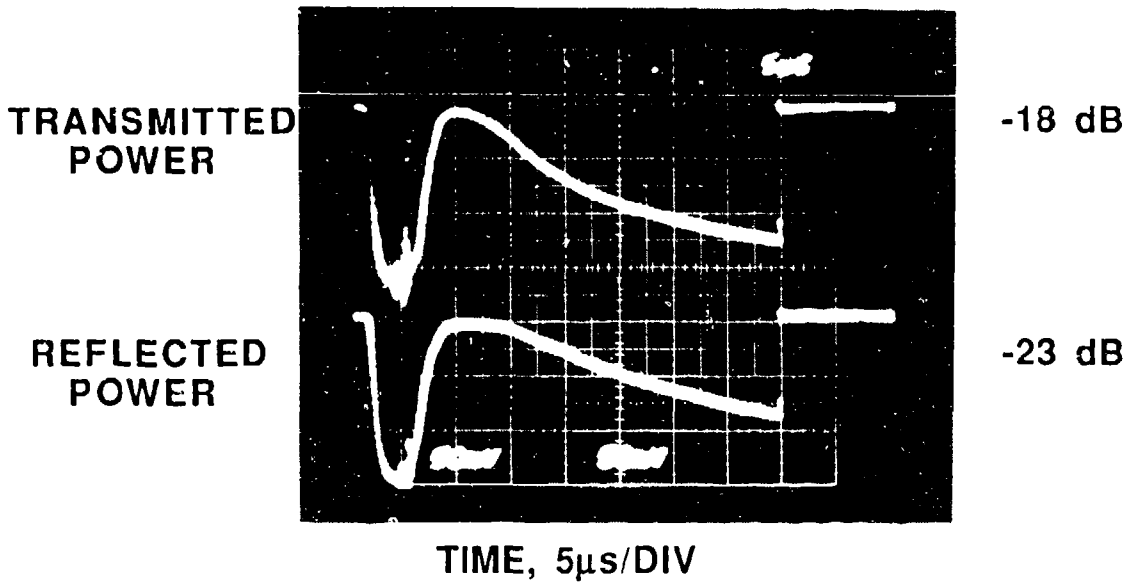

Figure 21 Cloaking demonstration. The 50-ohm load normally used to terminate the transmission system is replace with a short; microwave power reaching the short is reflected back toward the plasma-loaded waveguide. The EM-wave frequency was 4.95 GHz, the spark-gap current was 700 A (for each of the four five-gap spark arrays), and the electron collision frequency was 61 GHz.

We installed the spectrum analyzer to increase the dynamic range of the transmission system. The spectrum analyzer is operated as a tuned receiver by inhibiting the frequency sweep and manually setting the frequency. We then display the vertical output from the spectrum analyzer on an oscilloscope to obtain a temporal record of the microwave power as shown in Figure 22. The IF bandwidth on the spectrum analyzer is 3 MHz, which provides a temporal resolution of about 0.3 μs. The improvement in dynamic range is readily apparent. The baseline at the top of the photo is 0-dB attenuation, since this is the power level prior to pulsing the plasma. When the plasma is pulsed, the attenuation increases to 50 dB for a spark-gap current of 940 A. The noise at the bottom of the oscilloscope trace is the weak signal from the microwave source after it is amplified by the 10-dB power amplifier. The dynamic range for this system is now ≥70 dB.

We measured the attenuation of the microwave signal transmitted through the plasma as a function of the electron collision frequency. The collision frequency[17] is varied by changing the He-gas pressure. The data is shown in Figures 23 for microwave frequencies of 4, 5, and 6 GHz. The attenuation increases as the spark-gap current, and hence the plasma density, is increased. The attenuation increases because with higher electron densities, more electrons are available for acceleration by the EM wave. Another trend is that the attenuation decreases as the collision frequency increases. This is expected since the electron collision frequency is always greater than the microwave frequency in these experiments. These trends are predicted by the theoretical model as described in Section 2.

We also measured the attenuation as a function of the microwave frequency for different plasma densities as shown in Figure 24. The largest attenuation is observed for the lowest EM-wave frequency and the highest plasma density (i.e., spark-gap current). The attenuation decreases, at fixed microwave frequency, as the plasma density decreases. We also note that the attenuation decreases as the microwave frequency increases. These trends are consistent with those observed in Figure 23. We emphasize that there is no point where the attenuation saturates; it will continue to increase with increasing plasma density.

We measured the attenuation of the transmitted signal for different plasma-density profiles. We produced different profiles by pulsing selected 5-gap arrays. Our preliminary conclusion is that the shape of plasma profile has only a minor effect on the transmitted signal. We found that the maximum attenuation is provided by the densest plasma with the longest axial length.

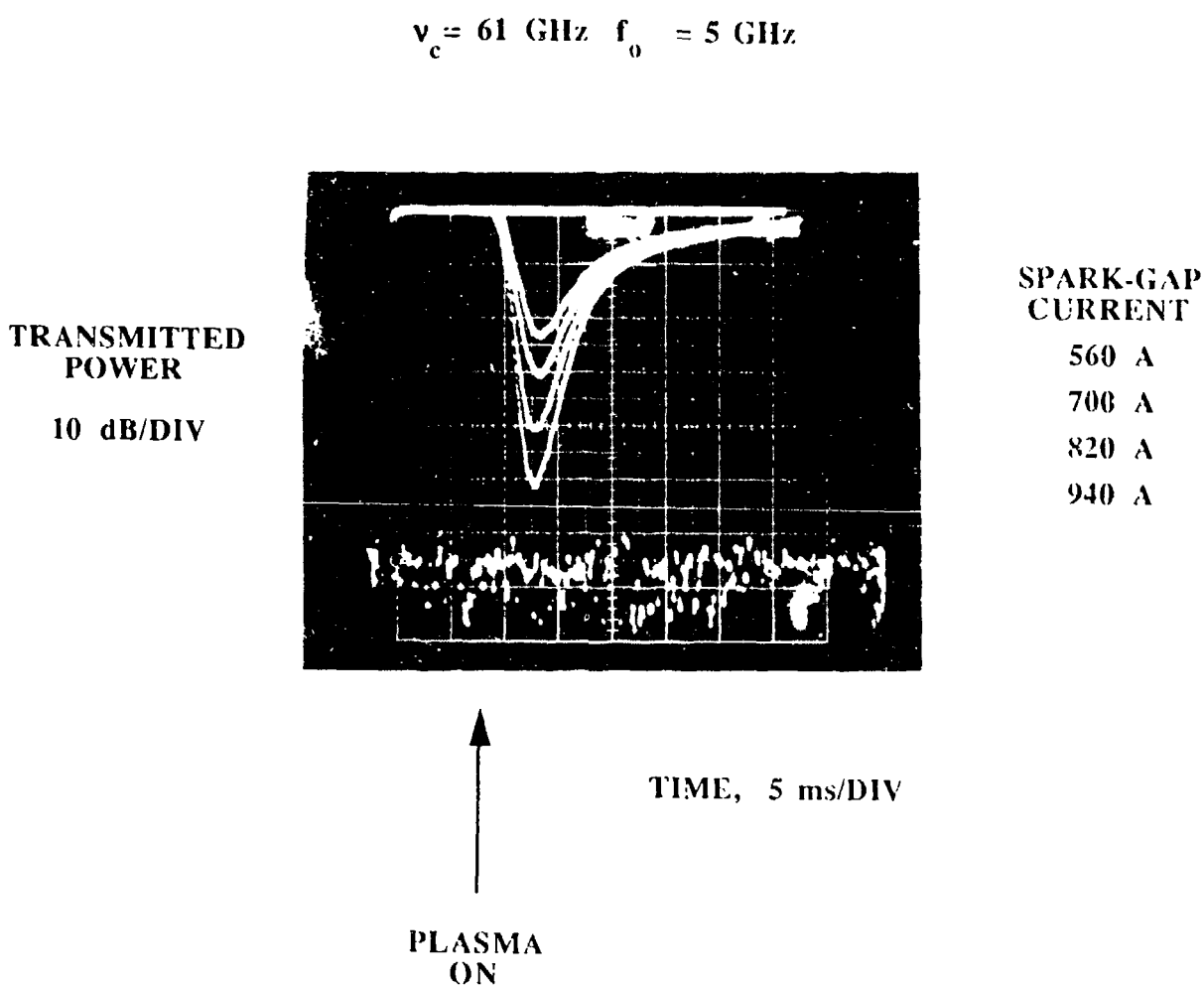

Figure 22 Attenuation of the transmitted signal measured using a spectrum analyzer operated as a tuned receiver. The line at the top of the trace is 0 dB attenuation. The EM-wave frequency was 5 GHz, and the electron collision frequency was 61 GHz.

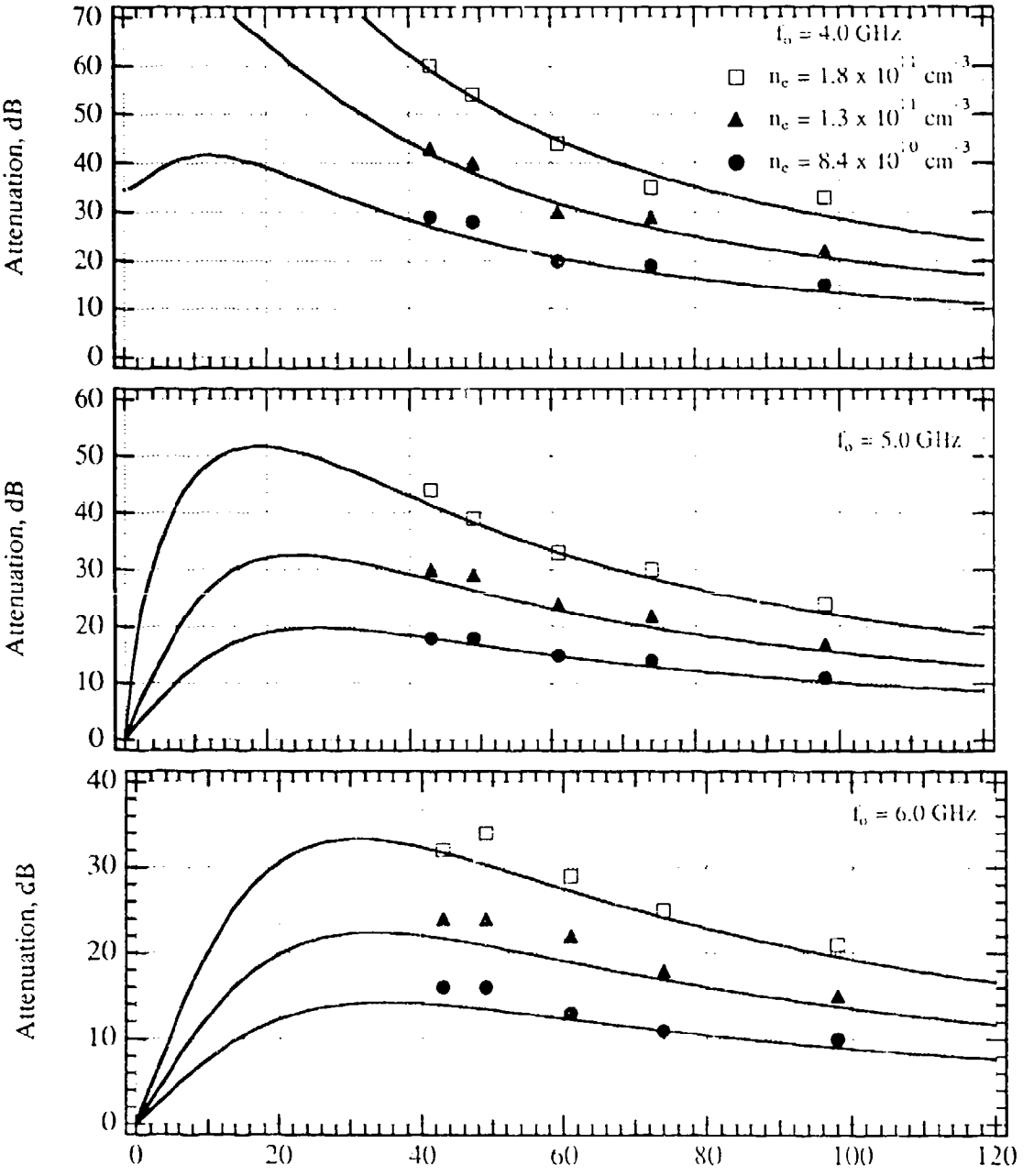

Figure 23 Attenuation versus collision frequency for plasma-filled waveguide. The absorption vs. collision frequency is measured in the plasma-filled waveguide experiment for several values of the radiation frequency and the plasma density. The solid curves represent the absorption as calculated from theory.

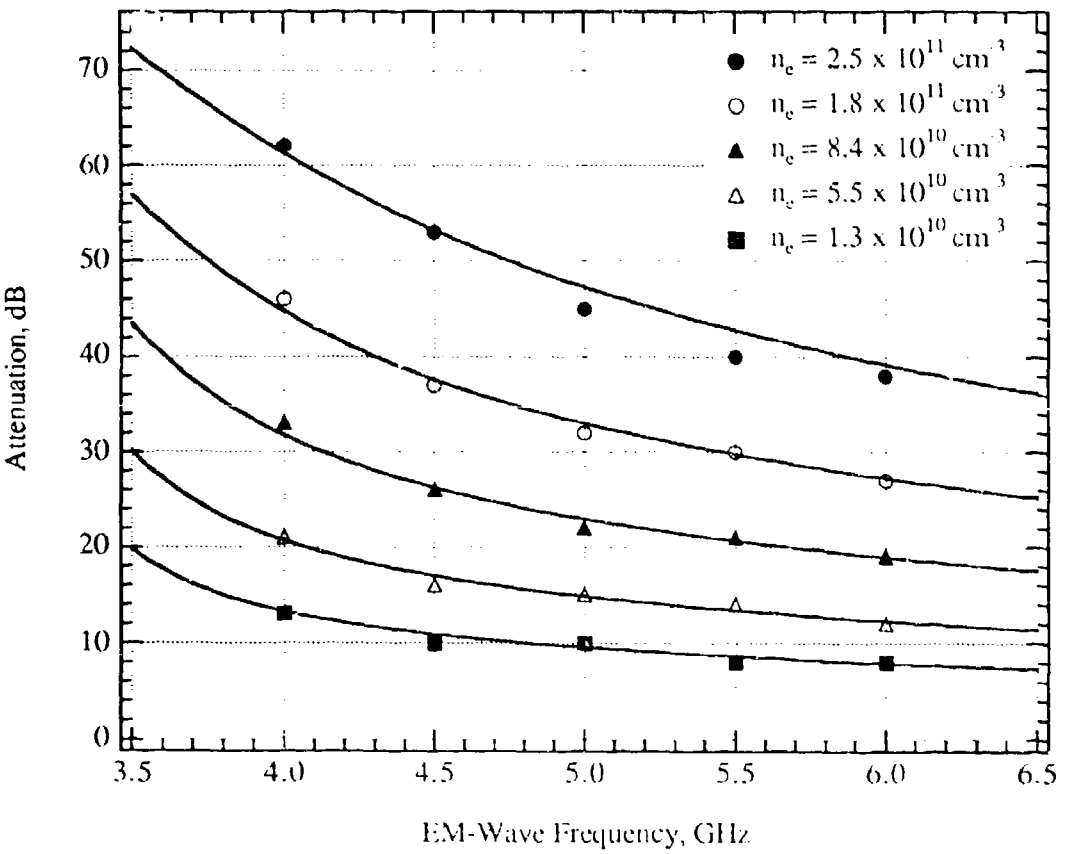

Figure 24 Attenuation versus microwave frequency in the plasma-filled waveguide. The absorption vs. EM-wave frequency is measured in the plasma-filled waveguide experiment for several values of the plasma density. The collision frequency is fixed at 60 GHz, which corresponds to a Helium gas pressure of 175 Torr. The solid curves represent the absorption as calculated from theory.

4.3.1. Comparison of Experimental Results With The Theoretical Model

We applied the theoretical analysis of Section 2 to the data in Figures 23 and 24 and achieved very good agreement. Using the profile shown in Figure 15, we modeled the electron-density profile as a 22-cm-long plasma of uniform density. However, since we did not have an absolute measurement of the electron density using the Langmuir probe, we used a self-consistent curve-fitting procedure to determine the electron density as described in Section 4.2.

We applied the theoretical model with the electron-density scaling shown in Figure 16 to the data in Figures 23 and 24. The theoretical curves are superimposed on the measured data in the figures. There is excellent agreement between experiment and theory. Also, since the data in Figure 23 was recorded independently of the data in Figure 24, these data provide an independent confirmation of the validity of the model and the scaling relationships.

5. EM-WAVE ABSORPTION BY A PLASMA-FILLED ENCLOSURE

In this section we describe the operation of a plasma-cloaking prototype consisting of a radar target and a plasma source inside a ceramic enclosure. The system's design is based on the principles described in the previous sections; in particular the plasma source and gas-handling system used in the plasma-filled waveguide experiments are redesigned for integration into the ceramic enclosure. The plasma cloaking principle was demonstrated by measuring the prototype's radar cross section (RCS) in a compact radar range that can measure far-field EM-wave interaction with the target without interference from other structures.

5.1. The Ceramic Enclosure

The ceramic enclosure system is pictured in Figure 25. The enclosure is 7" in diameter at its base and 18" long from base to tip. The wall thickness varies over the its length such that microwaves in the frequency range from 9.5 to 10.5 GHz pass through the wall with little reflection. This is known as the enclosure's transparency zone. A perforated circular plate is mounted inside the enclosure 4" from its base. The plate will serve as a reflector for incident radiation. Its radar cross section[18, 19] (RCS) is given by

$$\sigma_{RCS} = \frac{16\pi^3 a^4}{\lambda^2}\left(\frac{J_1(u)}{u}\cos(\theta)\right)^2 \qquad (27)$$

where a is the plate radius, λ is the radiation wavelength, θ is the observation angle with respect to the plate's normal vector and $u \equiv 4a\sin(\theta)/\lambda$. As seen in Figure 26, the peak RCS of 3.5 dBsm occurs for normal incidence and the RCS is relatively flat over a wide angular range; from θ=0 to 10°, the RCS varies by only 2 dBsm. The perforations allow the plate to be partially transparent to the UV radiation from the spark gaps according to the same principle used for the slotted waveguide in the plasma-filled waveguide experiments (See Section 4).

A spark-gap array is mounted 2" behind the reflector plate. Its purpose is to produce the UV radiation which will ionize the gas mixture inside the enclosure and create the plasma. The spark gaps, shown in Figure 27, are arranged into two circuits of 5 spark gaps each placed along a circular curve on a ceramic substrate. A high voltage lead is

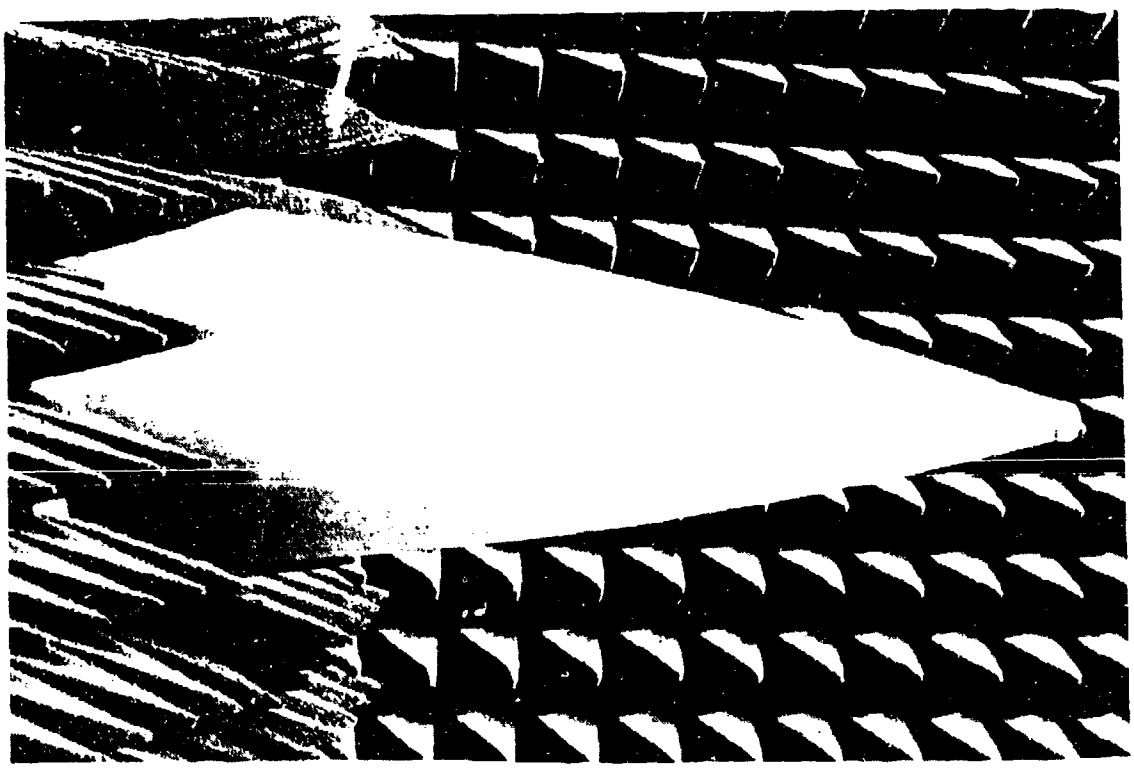

Figure 25. Plasma-filled ceramic enclosure

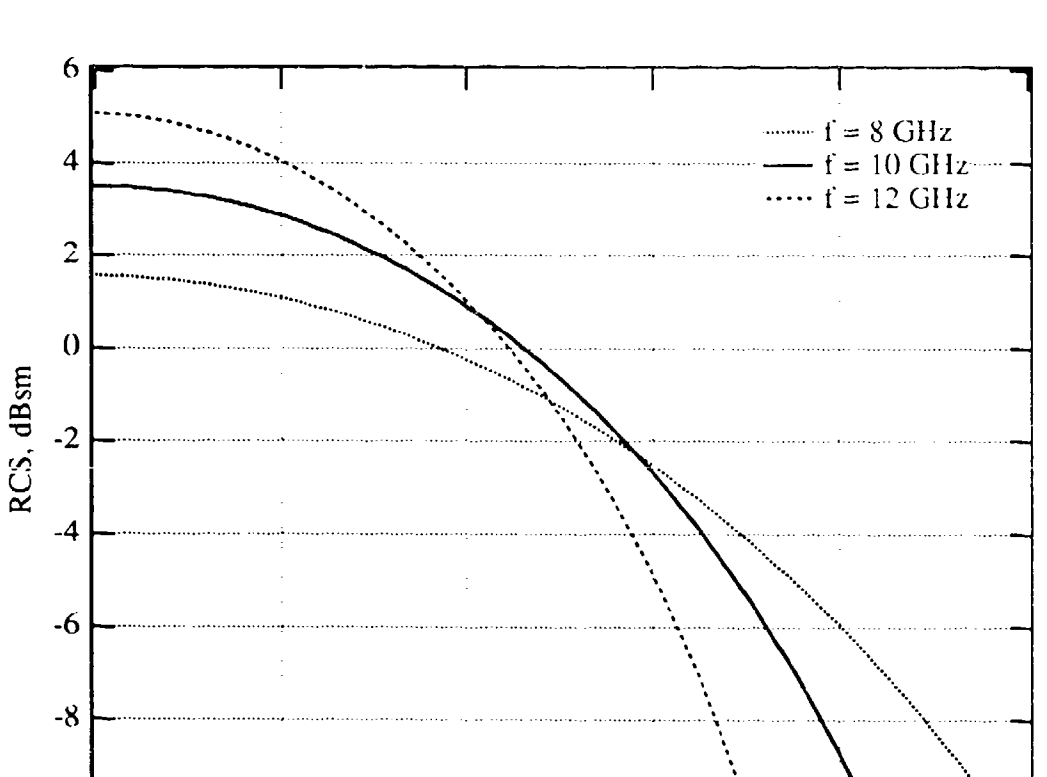

Figure 26. Radar cross section of circular plate. The RCS of the 5" diameter circular plate is calculated for a frequencies of 8, 10 and 12 GHz. It is seen that the RCS changes very little for angles of incidence less than 5° thus indicating that the alignment is not critical for RCS measurements.

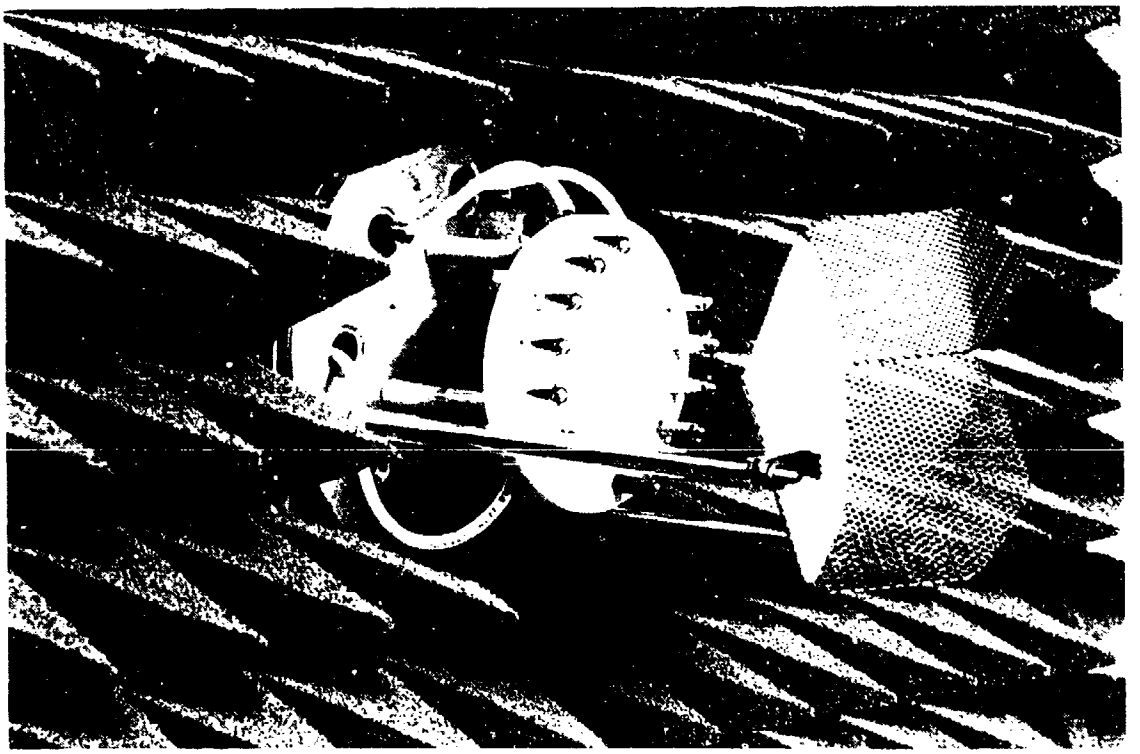

Figure 27. Spark gap assembly

connected to one end of the spark-gap array and a return line is attached to the other side. Switching is performed by a 20kV-100kA ignitron switch. When the high voltage is turned on, the large voltage difference on the spark gaps causes the gas mixture in the gap to break down, thus allowing current to flow from a bank of discharge capacitor through the spark gaps. In our experiments, a 1-μF capacitor, charged to 10 kV was connected to each spark-gap circuit. During the high-voltage pulse, the current reached a peak value of 3000 A in 4 μsec and then decayed with a half-life of 20 μsec. Each spark gap consisted of a 0.25" spacing between tips and each tip was made from 0.060" tungsten with a 40° cone ground on each end.

The spark-gap array and the reflector plate are mounted as an integral unit on the ceramic enclosure's back flange. The spacing between the components is critical because too-small a spacing would lead to high voltage breakdown occurring in undesired locations. High voltage feedthroughs for spark-gap operation, a vacuum pumping port, gas feedthroughs for maintaining the proper gas mixture and diagnostic feedthroughs for measuring plasma density and providing feedback on the device's operation are all mounted on the enclosure's back flange. When the device was operated inside the compact radar range, all connections except the high-voltage lines are valved off and disconnected in order to reduce spurious reflections that would reduce measurement's dynamic range and the effects of the plasma cloaking.

5.2. The Compact Radar Range

The compact radar range located at the Microwave Products Division of Hughes Aircraft was designed specifically for RCS and antenna measurements. Equipped with a March Microwave reflector system, this range provides test zones as large as to 6 feet over the frequency range of 4 to 100 GHz. The test zone, also called a quiet zone, is the area where the radiation pattern closely resembles a plane wave incident from a distant source, thus allowing far-field measurements to be made in relatively small spaces.

The chamber measures 25' wide by 19.5' high by 55' long and is fully lined with Rantec anechoic material which effectively absorbs any radiation at the walls and prevents multiple reflections from interfering with the measurement in progress. The chamber background levels within the 6' test zone are better than -55 dBsm from 4 to 8 GHz and -60 dBsm from 8 to 18 Ghz. Targets for RCS measurement are typically placed on a 10' high, low RCS, tapered foam column.
a)

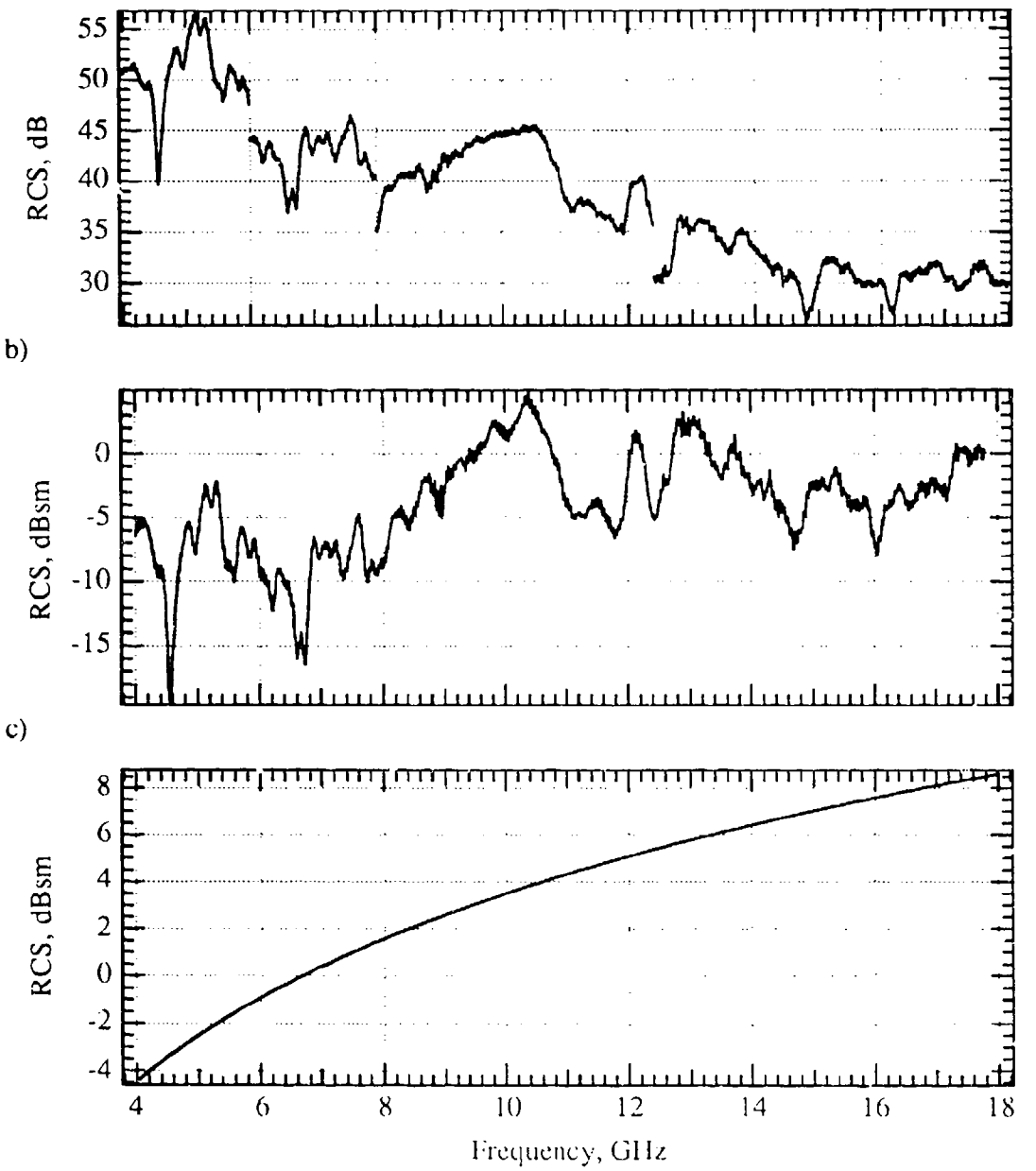

Figure 28. Ceramic enclosure RCS Calibration. In order to determine the absolute RCS of the enclosure system, we measured the radar return from the system with no plasma present as shown in a). The gaps in the data curves represent the gain differences in the horns used to produce the various segments. The data in a) is then compared to the return from an object of known RCS. in this case a 14" metal sphere was used. The result is the enclosure's absolute RCS shown in b) as dBsm. Figure c) plots the RCS for the microwave reflector within the enclosure.

The system electronics allow for a wide variety of measurements including RCS vs. time, frequency, down-range position and target orientation. Imaging is also possible via Fourier analysis of RCS vs frequency measurements

5.3. Calibration in the Radar Range

The enclosure's absolute radar cross section is determined by comparing its measured return to the return from a 14" metal sphere whose RCS is calculated to be nearly constant at -10.01 dBsm for frequencies above 2.8 GHz. Below 2.8 GHz, the sphere's RCS is dependent on frequency and shows the characteristic Mie resonance. As seen in Figure 28, the enclosure's absolute RCS has a very complex dependence on frequency. This is due to the structures on the back side, structures on the inside and multiple reflections when the incident frequency lies outside the transparency zone.

Since the plasma is enclosed inside the enclosure, it is not possible for it to cloak the structures on the outside and they will limit the possible RCS reduction. Figure 29 is a high-resolution range strobe of the enclosure system showing the radar return as a function of distance from the transmitter. It shows the relative return from various portions of the enclosure such as the tip, the internal reflector, the back flange and the rear structures. The high-resolution range strobe is determined by taking the fourier transform of a frequency strobe. The range resolution is $\Delta x = c/2\Delta f$ where Δf is the interval of the frequency strobe. In our example, the frequency was scanned from 8 to 12 GHz, therefore the range resolution is 1.5 inches.

It is apparent from the figure that the maximum return is from the reflector mounted inside the enclosure. In this plot, the return from the target is normalized to 0 dB. A local maximum of -40 dB corresponds to the enclosure's tip and the rear structures contribute to a broad maximum of -25 to -30 dB. It is not possible for the plasma to cloak the rear structures, therefore it is expected that the maximum effect of plasma cloaking is to reduce the RCS by 25 to 30 dB. We emphasize that the relative return from the various enclosure structures is dependent on the interval selected for the frequency strobe. A range strobe using a 4-to-8-Ghz interval will, in general, have a different profile from one using an 8-to-12-Ghz interval.

A similar strobe with the plasma turned on would provide a definitive graphic illustration of the plasma-cloaking effect. In principle, it would drive the return from the internal reflector to much lower levels while leaving the returns from the tip and the rear structures unaffected. Unfortunately, it was not possible to make such a measurement due to the plasma's short lifetime and low plasma pulse rate. There are two possible ways to make the high-resolution range measurement. In the first method, the plasma must stay on

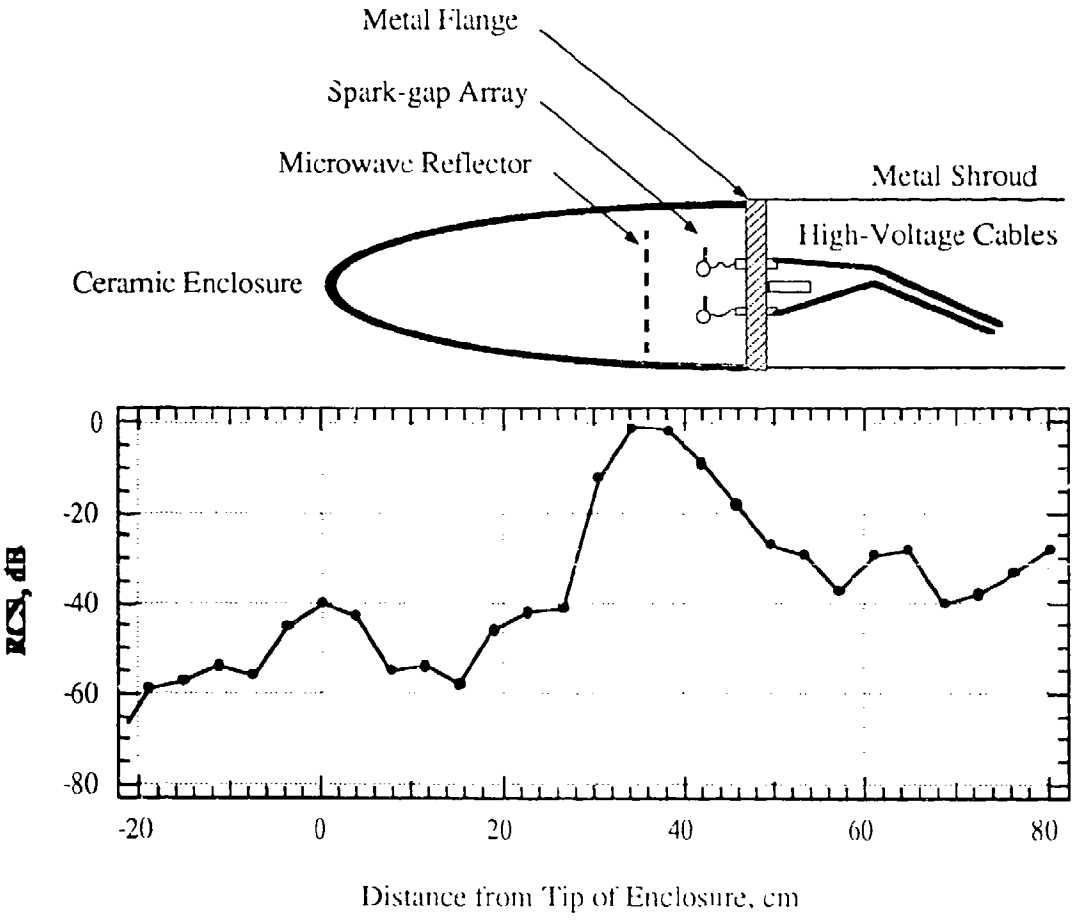

Figure 29. High-resolution range strobe of ceramic enclosure. A 1-d range strobe of the ceramic enclosure with the plasma OFF reveals that the microwave reflector is the biggest contributor to its RCS. Smaller contributions come from the tip (-40 dB), the metal flange (-20 dB) and the rear structures (-20 to -40 dB). Since it is impossible to use the plasma to attenuate signals from exterior structures, the plot range scan predicts that the RCS can be reduced by a maximum of 20 to 30 dB.

at a constant intensity for the duration of the range strobe, a minimum of 100 μsec. In the second method, the plasma is pulsed at the same rate as the radar transmitter whose minimum pulse rate is 1000 Hz. In our experiments, the plasma source is capable pulsing at a maximum of 1 Hz while the plasma density changes rapidly throughout its lifetime, thus making synchronization by either method impossible.

Additionally, a high-resolution range strobe with the plasma on could be performed by sending a radar pulse of very short duration and gating the receiver to look for the pulse at a time corresponding to reflection from a particular distance. By varying the gate timing, it would be possible to produce a return vs. distance measurement. The duration of the pulse must be as short as the desired resolution, i.e. $\Delta\tau = c/\Delta x$. For $\Delta x = 1.5"$ resolution, the pulse width must be 27 picoseconds, well beyond the capability of the MMS-300 radar system whose minimum pulse duration is 5 nanoseconds corresponding to a pulse length of 5 feet.

5.4. The Cloaking Measurement

As discussed in the previous section, it is necessary to synchronize the plasma source with the radar transmitter during a measurement. Therefore, the effects of the plasma cloaking vs. frequency are measured by single shot methods where each shot is made at a different frequency. Each measurement is made by transmitting a burst of radar pulses with a 400-kHz repetition rate throughout the plasma's lifetime. The return from each radar pulse is measured as a phase and an amplitude. Figures 30a and 30b show a typical set of data for the phase and amplitude of the radar return from the enclosure during a single plasma pulse. Each data point on the plots corresponds to a single radar pulse. During the time from 0 to 16 μsec, the plasma is turned off and the radar return is constant at -5 dBsm. At 16 μsec, the spark-gap current pulse is initiated and the plasma forms in the enclosure as evidenced by the decrease in RCS from -5 dBsm at 16 μsec to -27 dBsm at 20 μsec - an RCS reduction of 22 dB. Determination of the peak RCS reduction is affected by the low radar-pulse repetition frequency. The phase is likewise affected by the plasma formation.

Figure 30c plots the spark-gap current during the plasma pulse. When compared to the RCS measurement in Figure 30a, it is seen that plasma formation begins at the onset of the current pulse. However, the peak plasma density is achieved at a time delayed with respect to the peak spark-gap current because the plasma density accumulates throughout the current pulse due to a finite electron-ion recombination rate. If the recombination

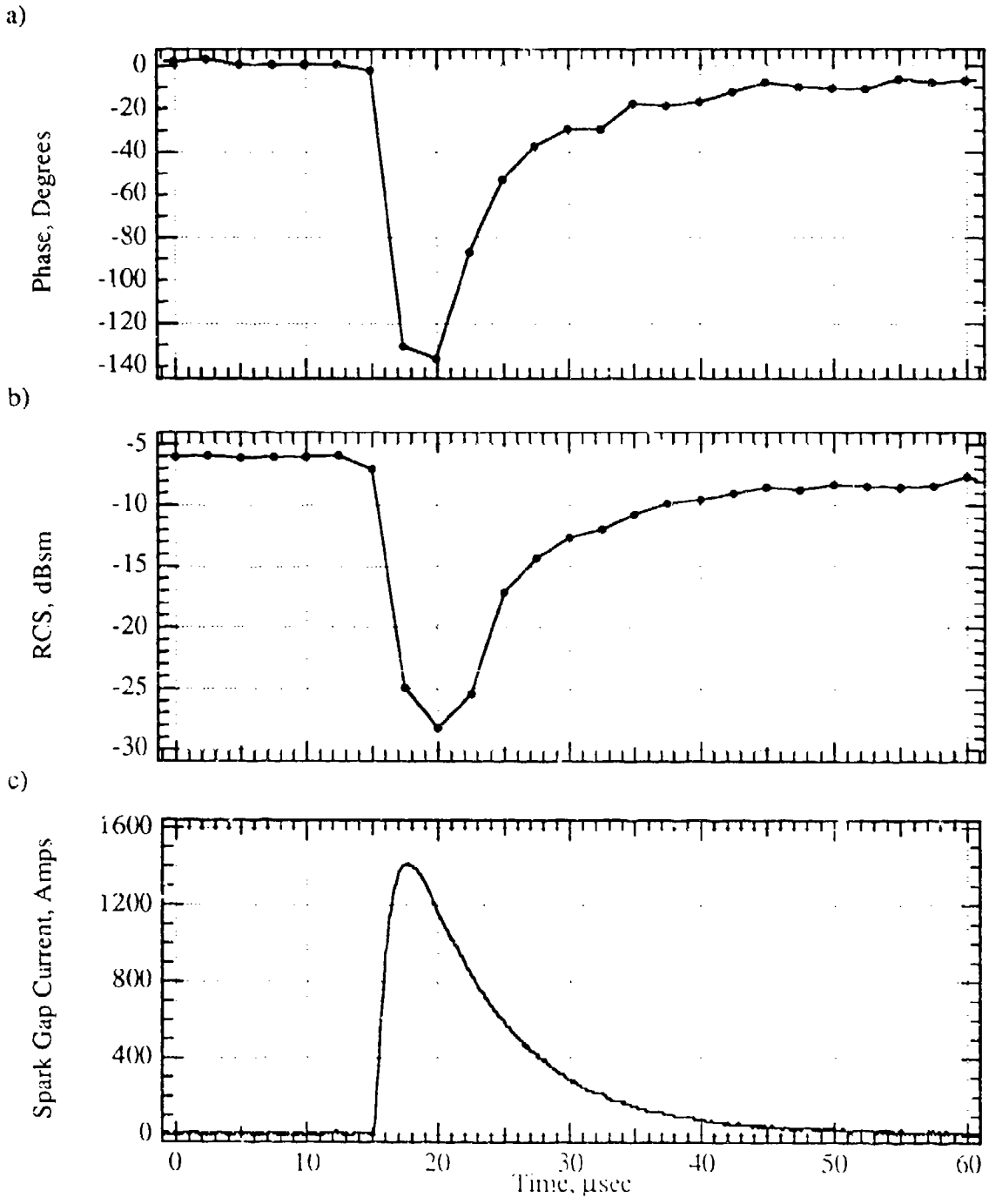

Figure 30. Single shot RCS measurement of plasma-filled enclosure. A typical data set for the radar return from the plasma-filled enclosure is plotted for a radar frequency of 9.25 GHz. As the spark-gap current is pulsed, the plasma density grows within the enclosure thus decreasing the RCS and phase shifting the return signal.

rate were zero, then the plasma density would increase whenever current flowed through the spark gaps and would never decrease.

Several sets of data such as the one shown in Figure 30 were produced covering the frequency range from 4 to 14 Ghz. Figure 31 displays the results of the measurements by plotting the peak RCS reduction vs frequency. There is considerable structure present in the graph; much of it is due to multiple reflections within the enclosure while a contribution is caused by resonances with external structures. The RCS reduction in the enclosure from 9 to 11 Ghz is relatively flat because that is the enclosure's transparency zone. In that range, the enclosure is designed to allow EM transmissions to pass through unhindered by reflections at the enclosure's surfaces, thus eliminating the possibility of multiple reflections. In principle, it would be possible to design the enclosure with the transparency zone anywhere.

When comparing Figures 31 and 8 it is not obvious why their should be so many peaks in the enclosure's RCS reduction. After all, Figure 31 and Equation (24) show that the resonant absorption only occurs for coincident choice of the plasma parameters and the front-interface reflectivity. A simple explanation is that the plasma density is neither constant nor uniform within the enclosure. As the density rises to its peak, both the real and imaginary parts of the EM-wave propagation constant are changing, thus making it more likely to satisfy the conditions for resonant absorption. The other feature of Figure 31 seeking explanation are the dips in the enclosure's RCS reduction. If we assume that the ambient extraneous reflectivity is -20 dB, then most of the dips are within the range of 6 dB from that and may be explained as part of the internal reflections model.
Some of the dips extend much farther than 6 dB and they are probably due to multiple reflections from external structures.

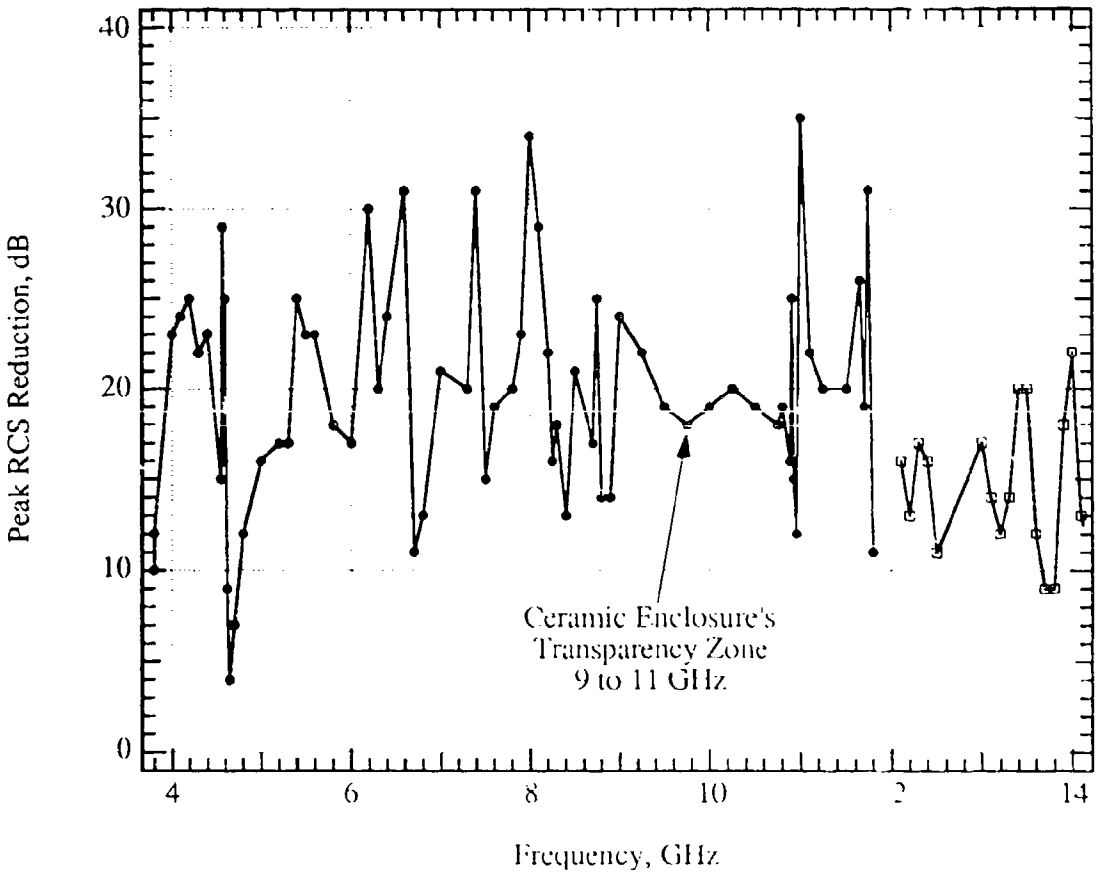

Figure 31. RCS reduction vs frequency for the plasma-filled enclosure. The RCSR is relatively flat in the enclosure's transparency zone (9 to 11 GHz), but there is substantial structure elsewhere due to interference between multiple reflections within the enclosure and the external structures. The RCS averages to a nominal value of ~20dB over the frequency band which is in agreement from the range strobe data of the enclosure system that showed that the external structures had a radar return 20 to 30 dB below the microwave reflector's.

6. REFERENCES

1. Ginzberg, V.L. *The propagation of electromagnetic waves in plasmas* (Pergammon Press, New York, 1970).
2. Vidmar, R.J. *Generation and properties of tenuous plasma bodies at atmospheric pressure* , Annual Report, AFOSR Contract No. F49620-85-K-0013 (SRI International, 1988).
3. Vidmar, R.J. *IEEE Plas.Sci.* **18**, 733 (1990).
4. Vidmar, R.J. *Plasma cloaking: air chemistry, broadband absorption and plasma generation*, Final Report, AFOSR Contract No. F49620-85-K-0013 (SRI International, 1990).
5. Stenzel, R.L., A.Y., W. & Kim, H.C. *Phys. Rev. Lett.* **32**, 654 (1974).
6. Huddlestone, R. & Leonard, S. *Plasma diagnostic techniques* (Academic Press, New York, 1965).
7. Mathews, J. & Walker, R.L. *Mathematical Methods of Physics*. 1-501 (Benjamin/Cummings, Menlo Park, CA, 1970).
8. Budden, K.G. *The propagation of radio waves* (Cambridge University Press, Cambridge, 1985).
9. Yariv, A. *Introduction to Optical Electronics*. 1-342 (Holt, Rinehart and Winston, Inc., New York, NY, 1971).
10. Lind, R. *Investigation of Ultraviolet photoionization sustained discharge for gas lasers*, Final Report, Contract No. N00014-73-C-0287, (Hughes Research Labs, Malibu, CA, 1976).
11. Weissler, G.L. in *Encyclopedia of Physics* (eds. Fluuge, S.), p. 323, (1956).
12. Schonhuber, M.J. *IEEE Trans. Power Apparatus and Systems* **88**, 100 (1969).
13. Cookson, A.H., Proc. IEE, **117**, p.269 (1970).
14. Hopkins, D.B. *Design considerations and data for gas-insulated high voltage structures* (IEEE, 1975).
15. Chen, C.C. *IEEE Trans. Micro. Theory and Tech.* **MTT-21**, 1 (1973).
16. Eisenhart, R. (1989).
17. Itikawa, Y. *Physics of Fluids* **16**, 831-835 (1973).
18. Knott, E.F., J.F., S. & Tuley, M.T. *Radar Cross Section* (Artech House, Denham, MA, 1985).
19. Tuck, G.T. *Radar Cross Section Handbook* (Plenum Press, New York, 1970).

ACKNOWLEDGMENTS

Numerous people contributed to the success of this program. The authors of this report would like to extend our thanks and gratitude to Roland Fleig, Hayden Gallagher and Karl Troesken of the Hughes Research Labs for their innovative ideas and relentless troubleshooting. Thanks to Robin Harvey , also of HRL, Dave Whelan of RSG and Jay Palmer, now at NOAA, for illuminating discussions that lead to experimental realities. Bob Eisenhart of HAC's Missile Systems Group was instrumental in making this program proceed with ease; we would like to acknowledge his invaluable expertise that he applied to designing and fabricating the slotted waveguide used in the plasma-filled waveguide experiments. He also donated the ceramic enclosure for the plasma-filled enclosure experiments. Several people at the Radar Systems Group supplied fantastic services to us while we conducted the RCS measurements at the compact radar range. They are Don Williams, Edwin Lee and Ray Santos. Our thanks to all.